Sea ice motion from satellite passive microwave imagery assessed with ERS SAR and buoy motions

R. Kwok,[1] A. Schweiger,[2] D. A. Rothrock,[2] S. Pang,[1] and C. Kottmeier[3]

Abstract. Observing the motion of sea ice from space is analogous to observing wind stress over the wet oceans; both provide surface forcing for modeling ocean dynamics. Ice motion also directly provides the advective component of the equations governing the mass balance of the sea ice cover. Thus its routine observation from space would be of great value to understanding ice and ocean behavior. To demonstrate the feasibility of creating a global multidecadal ice motion record from satellite passive microwave imagery and to quantitatively assess the errors in the estimated ice motions, we have tracked ice every 3 days in the Arctic Ocean and daily in the Fram Strait and Baffin Bay during the 8 winter months from October 1992 to May 1993 and daily in the Weddell Sea during the 8 winter months from March to October 1992. The method, which has been well used previously, involves finding the spatial offset that maximizes the cross correlation of the brightness temperature fields over 100-km patches in two images separated in time by from 1 to 3 days. The resulting ice motions are compared with contemporaneous buoy- and SAR-derived ice motions. The uncertainties in the displacement vectors, between 5 and 12 km, are better than the spatial resolution of the data. Both 85-GHz data with 12-km spatial resolution and 37-GHz data with 25-km resolution are tracked. These trials with the 37-GHz data are new and show quite surprisingly that the error is only about 1 km larger with these data than with the 12-km 85-GHz data. Errors are typically larger than average in areas of lower ice concentration; in the most dynamic regions, particularly near the ice edge in the Barents and Greenland Seas; and in zones of high shear. These passive microwave ice motions show a large increase in spatial detail over motion fields optimally interpolated from buoy and wind observations, especially where buoy data are virtually absent such as near coasts and in some passages between the Arctic Ocean and its peripheral seas. The feasibility of obtaining ice motion from the 37-GHz data in addition to the 85-GHz data should allow an important record of ice motion to be established for the duration of the scanning multichannel microwave radiometer (SMMR), special sensor microwave/imager (SSM/I), and future microwave sensors, that is, from 1978 into the next millenium.

1. Introduction

The circulation of sea ice determines the advective part of the ice balance and provides a velocity boundary condition on the ocean surface. The spatial gradient of this circulation, ice deformation, controls the abundance of thin ice and therefore the many surface processes dependent on thin ice, such as turbulent heat flux to the atmosphere and salt flux into the ocean. Convergent motion increases the local ice cover mass by rafting and ridging. Sea ice motion is readily observed in satellite imagery, the scale of the observed motion being dependent on the spatial resolution of this imagery. In recent years a number of procedures [*Fily and Rothrock*, 1987; *Kwok et al.*, 1990; *Emery et al.*, 1991] have been developed to recognize common features in various types of sequential images to ob-

tain displacement measurements. The quality of these measurements depends more on geometric fidelity and image resolution than on a thorough physical understanding of the ice signatures themselves. Imagery acquired by synthetic aperture radars (SAR) and the advanced very high resolution radiometer (AVHRR) are of particular importance for motion observations. The European Remote Sensing Satellites (ERS-1 and ERS-2), the Japanese Earth Resources Satellite (JERS-1), and the Canadian RADARSAT satellite all carry SARs; successive high-resolution SAR imagery (≈ 10–100 m) can provide almost all-weather, diurnal observations of ice motion. Prior to RADARSAT, large-scale motion measurements were limited by the narrow SAR swath widths, about 100 km. The wide-swath mode (500 km) of RADARSAT provides routine mapping of the Arctic in <3 days. To date, the SAR data records of the polar oceans, since the launch of ERS-1 in 1991, are still fairly sparse because of limitations in swath width, orbit geometry, and lack of onboard tape recorders on the ERS satellites. AVHRR imagery provides wide-swath observations (1000 km) at moderate resolution (≈ 1 km), but there are spatial gaps in the parts of the ice cover obscured by clouds [*Emery et al.*, 1991]. The AVHRR record provides more extensive coverage of the polar regions and dates back to 1981.

It has recently been demonstrated that despite its antenna

[1] Jet Propulsion Laboratory, California Institute of Technology, Pasadena.

[2] Polar Science Center, Applied Physics Laboratory, College of Ocean and Fisheries Sciences, University of Washington, Seattle.

[3] Universität Karlsruhe Institut für Meteorologie und Klimaforschung, Karlsruhe, Germany.

Table 1. EFOV of the Relevant SSM/I Radiometer
Channels

Frequency, GHz	EFOV, km
37.0	38 × 30
85.5	16 × 14

EFOV, effective field of view; SSM/I, special sensor microwave/
imager.

footprints of 10 or more kilometers, sequential imagery from
85-GHz special sensor microwave/imager (SSM/I) can provide
ice motion observations [*Agnew et al.*, 1997; *Liu et al.*, 1998].
We demonstrate here that one can obtain ice motion from the
37-GHz data as well. This offers an extraordinary opportunity
to create an ice motion data record starting in 1978 with the
scanning multichannel microwave radiometer (SMMR), which
had a 37-GHz channel but no 85-GHz channel and continuing
through the present and indefinitely into the future with
planned SSM/I and other passive microwave radiometers.
These measurements would be complementary to the higher-
resolution satellite observations described above.

The objective of this paper is to provide a quantitative as-
sessment of the ice motion observations obtained with 85-GHz
SSM/I and with 37-GHz SMMR data. The utility of these
measurements depends on an understanding of the errors in
displacement estimates. Our approach is to characterize these
uncertainties by comparing the derived motion with available
buoy and ERS SAR-derived ice motions. In the following
section the ice motion tracking procedure used to obtain the
displacement estimates is described, including the temporal
sampling issues of ice motion and the filtering of outliers. In
section 3 we compare 8 months of ice motion from the Arctic
and 8 months of ice motion from the Antarctic with buoy and
SAR ice motions. In section 4 we examine spatial features
visible in bimonthly mean drift patterns computed from the
results of section 3. One of the best long-term records of Arctic
ice motion comes from optimally interpolated buoy motions
augmented by surface geostrophic wind fields [*Rigor and
Heiberg*, 1997]. Section 4 also shows a comparison between
these buoy-wind-derived motion fields and those from SSM/I.
The latter show interesting spatial details missing in the
smoothed buoy/wind fields. Summary remarks are given in
section 5.

2. Ice Motion Tracking

2.1. Description of Tracker

The inputs to the ice motion tracker are sequential SSM/I
brightness temperature fields (obtained from the National
Snow and Ice Data Center) mapped onto rectangular grids in
a polar stereographic projection. The SSM/I instrument has a
swath width of 1394 km, and observations are made at an angle
of incidence of ~53° at the Earth's surface. The gridded daily
brightness temperature fields are synthesized from data col-
lected from ascending and descending orbits. The 37-GHz
daily averages are binned, using a nearest neighbor scheme, to
square pixels with dimensions of 25 × 25 km and the higher-
resolution 85-GHz observations are binned to 12.5- × 12.5-
km-size pixels. Brightness temperatures observed over a 24-
hour period (midnight to midnight UT) are summed then
divided by the total number of observations to obtain an aver-
age brightness temperature at that pixel. Regions of open

ocean are masked out using analyzed fields of ice concentra-
tion derived from the same passive microwave observations.
Missing data values are replaced by the median value in the 3-
× 3-pixel neighborhood of that pixel. Sea ice displacements are
obtained by a motion tracker that identifies common features
in the successive brightness temperature fields. The procedure
used here is based on the algorithm described by *Kwok et al.*
[1990]. This routine was originally developed for production of
ice displacement fields from SAR imagery. Only an overview of
this tracking approach is given here. Instead, we provide a
more detailed account of issues associated with tracking ice
motion in passive microwave data.

In the motion tracker the magnitude of the normalized
cross-correlation coefficient is used as the measure of similarity
between features in the passive microwave data sets. The
method, which has been well used previously, involves finding
the spatial offset that maximizes the cross-correlation coeffi-
cient of the brightness temperature fields of features in two
images separated in time. Features are $n \times n$ pixels of bright-
ness temperature arrays that we extract from an image. Start-
ing with an approximate location on the second image, we
compute the correlation coefficient between an array from the
first image and an array of the same size on the second image.
This correlation value is recorded. The computation is re-
peated at each position as the array from the first image is
shifted on a two-dimensional grid to obtain an array of corre-
lation coefficients. The peak of this sampled surface is re-
garded as the location of maximum similarity between the
arrays from the two images. The displacement vector is then
given by the difference in geographic location of the centers of
the two arrays. This procedure is repeated for each feature
extracted from the first image. The process involves two dif-
ferent steps which utilize this image matching procedure: the
first step is performed at the nominal resolution to find the
approximate location of these features and the second step
focuses on refinement of the location of these features in the
oversampled data set (discussed below). Fast Fourier trans-
forms are used to improve the efficiencies in the computation
of these correlation surfaces. After each step, filters are used to
discard outliers and inconsistent displacement vectors based
on the statistics of the displacement field. Details of these filter
can be found in work by *Kwok and Cunningham* [1993]. After
the outliers are removed, there are holes in the output field.
We do not interpolate to fill them. Below, we describe three
modifications to this process for measuring displacements in
the passive microwave data.

2.1.1. Location of correlation peak. Oversampling of the
correlation surface could be used to provide subpixel location
of the correlation peak. If the input data are optimally sam-
pled, we should be able to estimate the peak location to better
than the nominal spatial resolution of the sensor (see Table 1).
An alternative to oversampling the correlation surface is over-
sampling the input data, and this is the more efficient approach
when the data volumes are small as is the case here. Either
approach should give the same results. In our implementation
we use an oversampling factor of 6 for the input data, resulting
in a sample pixel spacing of ~2.1 km for the 85-GHz data and
4.2 km for the 37-GHz data. With this oversampling factor, the
uncertainty in the location of the peak of the correlation sur-
face is determined by the pixel spacing of the oversampled
data. Even with an oversampling factor of 6, the quantization
noise of several kilometers is still significant for each vector
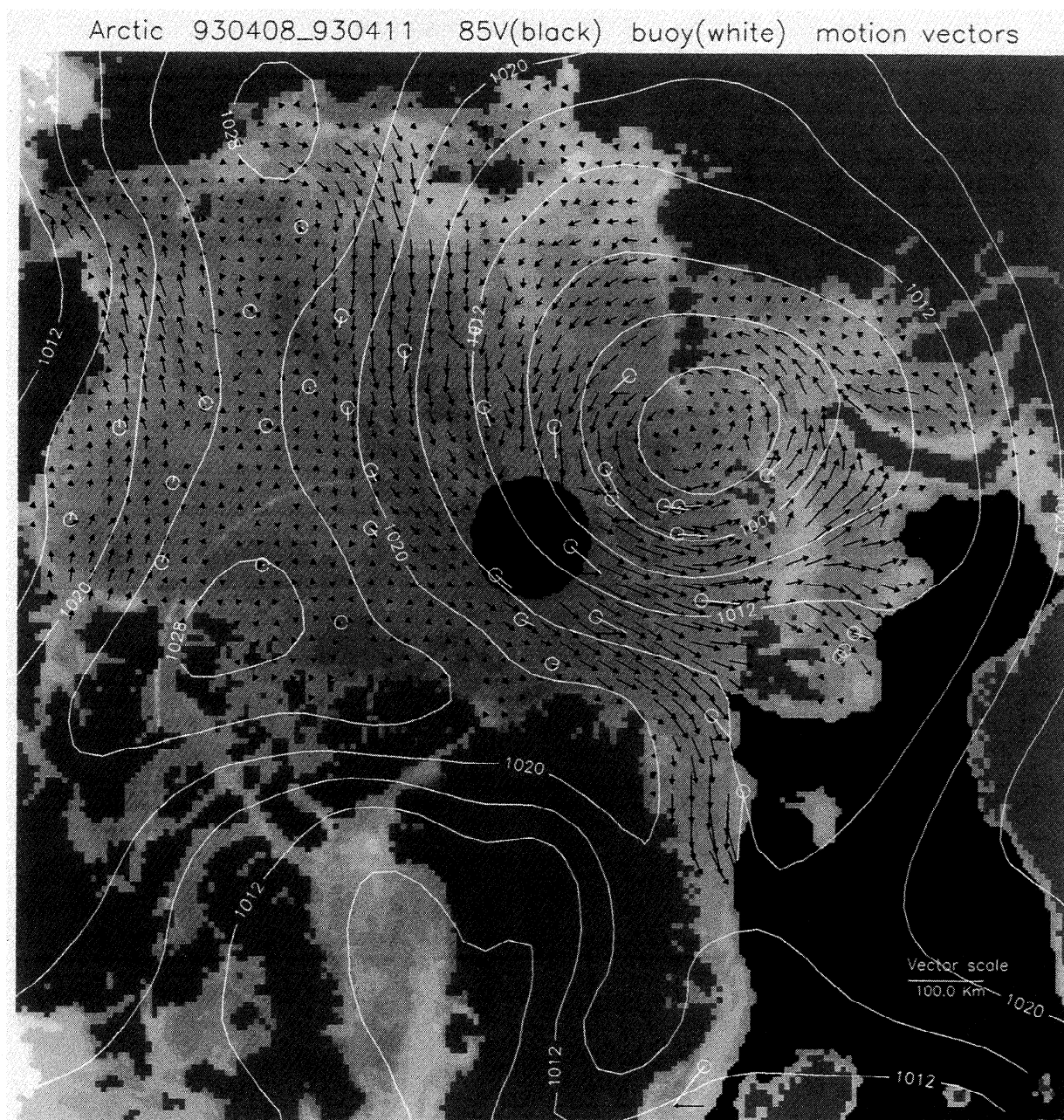observation. To reduce the uncertainty due to sampling, the

Figure 1. Three-day ice motion in the Arctic Basin from 85-GHz passive microwave data. Contours are isobars overlaid on the motion field. Three-day buoy motions are shown in white. The pressure contour interval is 4 mbar. The grid spacing is 80 km.

subpixel location of the peak is estimated using the eight neighborhood correlation values around the peak of the sampled correlation surface. A biquadratic surface of the form $f(x, y) = \Sigma_{i=0}^{8} a_i x^i y^i$ is fit to the nine correlation values; the maxima of the function are then computed using the method of steepest descent. This effectively reduces errors caused by spatial sampling of the correlation surface. This combination of oversampling factor and interpolation is a compromise between data volume and computational throughput.

2.1.2. Weather/surface change filter. The normalized correlation coefficient as a measure of similarity is insensitive to the absolute brightness levels of the arrays or features being compared. Both the 85- and 37-GHz channel observations are affected by clouds, atmospheric water vapor content, and changes in surface conditions (such as snow properties), and fairly significant changes in brightness temperature levels are associated with some of these phenomena. To avoid the detection of a false match between features using solely the normalized correlation coefficient, a match between features has to satisfy an additional condition that the difference between the mean brightness temperature levels of the two arrays is <10% of the observed brightness temperature. This threshold, which is a rather arbitrary choice, seems to be effective in removing areas that are dissimilar in brightness temperature or contaminated by atmospheric emissions. We find that this filter typically removes one to two observations per vector field. At times when there is severe weather, especially in the Weddell Sea, it could remove erroneous motion estimates from a large region.
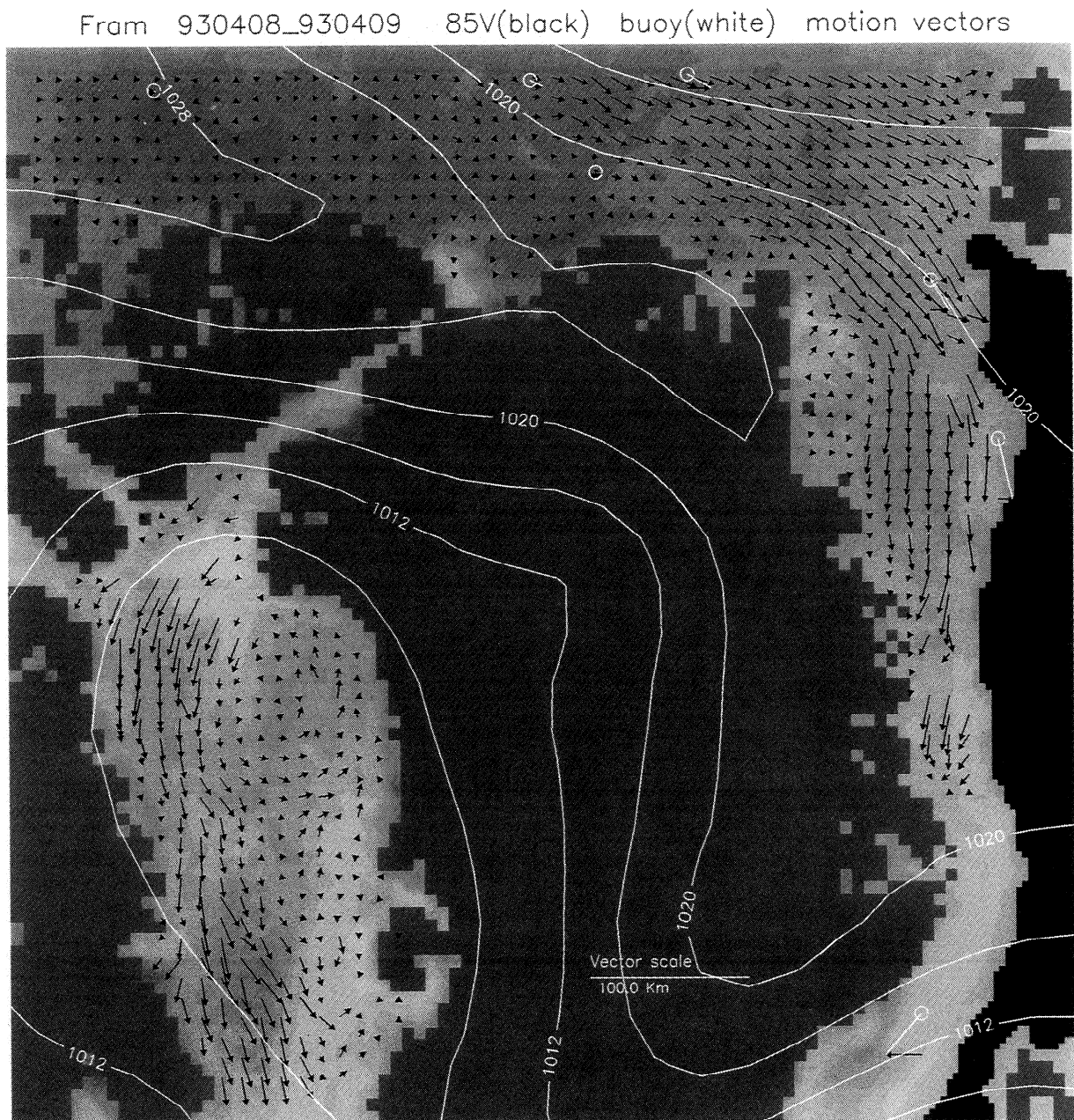
Figure 2. One-day ice motion in the Fram Strait and Baffin Bay and surroundings from 85-GHz passive microwave data. Contours are isobars overlaid on the motion field. One-day buoy motions are shown in white. The pressure contour interval is 4 mbar. The grid spacing is 40 km.

2.1.3. Filtering of outliers. The output displacement vector fields are further filtered using the wind field. We use the wind direction to constrain the direction of the output vectors. Displacement vectors that are not within 90° of the wind direction are discarded. The tolerance of this filter is set rather high because of uncertainty in the quality of the wind fields and because ice motion is not entirely wind driven. We use the reanalyzed wind fields from the National Center for Environment Prediction for this purpose.

2.2. Sampling Issues

Although the SSM/I products provide daily maps of the polar regions, the coarse resolution of the sensor limits the observability of displacements that are comparable to the footprint (Table 1). In other words, the resultant field would be quite noisy if we attempt to derive daily ice motion fields in the winter Beaufort Sea where the climatologically mean sea ice motion is between 2 and 5 km/d, small compared to the 12–15-km sensor resolution. Lengthening the time separation would enlarge the signal (displacement relative to the noise, resolution). Another consideration, however, is the change in the passive microwave signature of the features being tracked. The temporal correlation of the data tend to decrease as the areal fraction of sea ice types change with time due to advection, opening/closing, and ice growth. The determination of the temporal sampling interval of the motion field should be based on a balance of these factors.
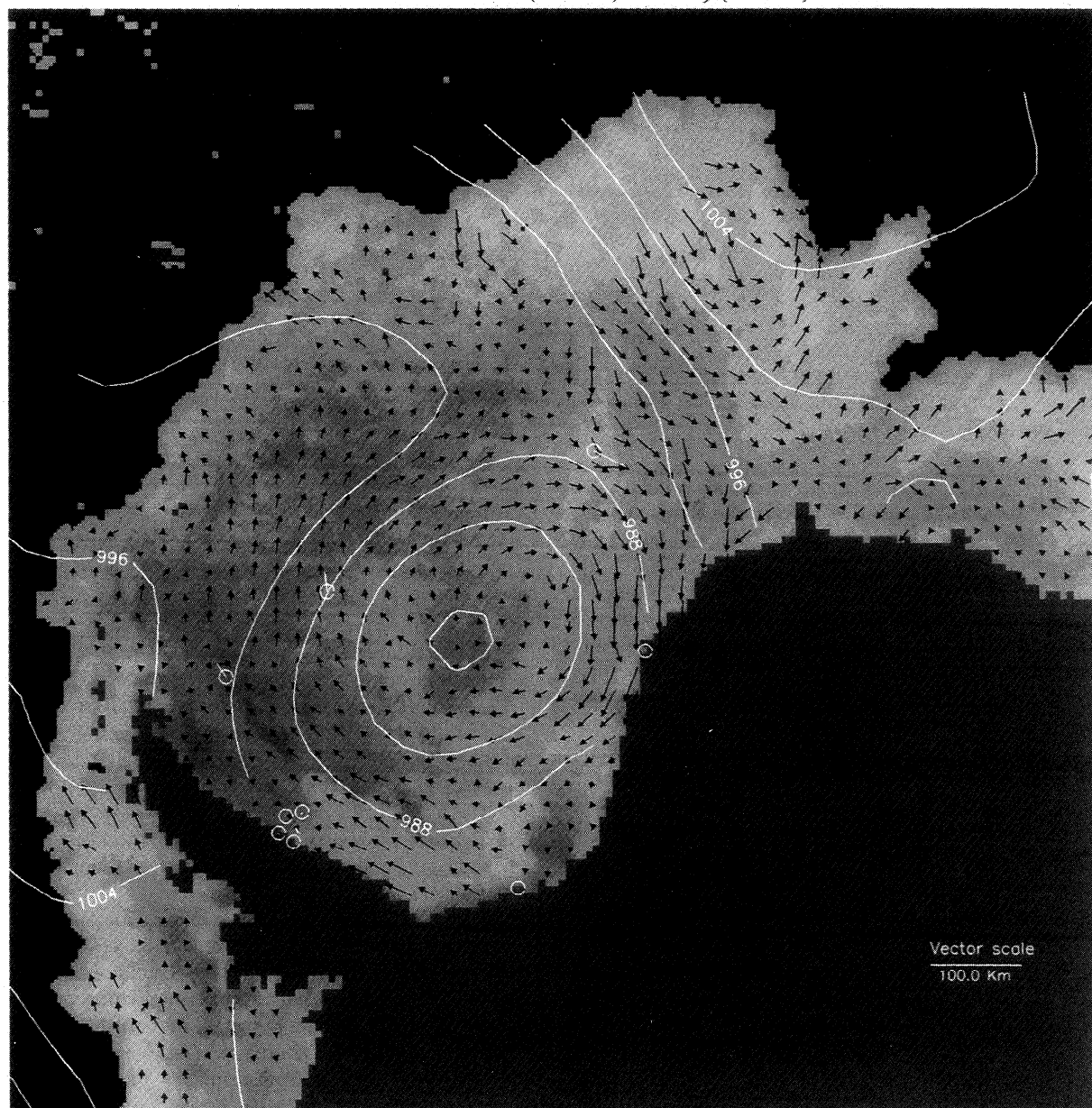
Figure 3. One-day ice motion in the Weddell Sea from 85-GHz passive microwave data. Contours are isobars overlaid on the motion field. One-day buoy motions are shown in white. The pressure contour interval is 4 mbar. The grid spacing is 80 km.

Our approach is to subset the daily SSM/I products into different regions such that the sampling interval of these displacement fields are based appropriately on the expected motion of sea ice in these regions. In the comparisons and examples that follow we use 1- and 3-day sampling intervals for ice motion in two regions of the Arctic and one in the Weddell Sea.

2.3. Summer Ice Motion

Summer passive microwave data are typically not suitable for ice motion observations because of the opacity of the atmosphere during these months (June–September in the Arctic and November–February in the Antarctic). The observed 85- and 37-GHz brightness temperatures tend to have large con-

tributions from the atmospheric emissions due to the increase in water vapor and cloud liquid water content in the summer. Melt/freeze cycles also increase the variability of surface emissivity. The derived ice motion, on the basis of our approach, tends to be unreliable between the onset of melt in the spring and freeze in the fall. This introduces a gap in the annual ice motion record which needs to be filled by some other means. In the following section we restrict our attention to passive microwave ice motion estimates from the winter months.

2.4. Regional Motion Fields

We select three regional subsets of data from the gridded brightness temperature fields for our illustration here and for our comparative analysis in the next section. The first region

Table 2. Comparison of 85-GHz Ice Motion With Buoy Motion for October 1992 to May 1993 (Arctic) and March 1992 to October 1992 (Antarctic)

Region	Channel, GHz	Interval, days	Δ, km	e_x, km	e_y, km	θ, km	Scale	ρ	Number of Points
			All Points						
Arctic	85 V	3	−1.0 (11.1)	1.1 (8.9)	0.8 (10.8)	0.5 (46.5)	6.6 (47.1)	0.76	2119
	85 H	3	−0.9 (11.7)	1.2 (9.9)	1.2 (11.2)	3.0 (50.4)	6.7 (49.2)	0.72	2097
Fram Strait/Baffin Bay	85 V	1	0.5 (5.3)	0.3 (4.3)	0.2 (5.2)	−2.7 (65.4)	4.2 (9.5)	0.76	1054
	85 H	1	0.3 (6.0)	0.4 (4.7)	0.8 (6.0)	1.7 (66.7)	4.6 (13.3)	0.67	1028
Weddell Sea	85 V	1	2.1 (7.8)	0.6 (7.4)	0.1 (8.2)	1.7 (59.6)	2.5 (7.8)	0.67	1553
			Excluding Points With Small Displacements						
Arctic	85 V	3	−1.2 (6.7)	0.9 (7.3)	0.7 (7.8)	1.7 (30.6)	1.0 (0.4)	0.86	1440
	85 H	3	−1.1 (7.5)	0.6 (8.5)	0.9 (7.9)	3.2 (32.8)	1.0 (0.4)	0.83	1419
Fram Strait/Baffin Bay	85 V	1	0.4 (3.9)	0.3 (4.7)	−0.4 (5.0)	2.8 (29.8)	1.1 (0.4)	0.84	222
	85 H	1	0.1 (4.0)	0.0 (4.8)	0.0 (5.1)	−4.2 (31.5)	1.0 (0.4)	0.83	205
Weddell Sea	85 V	1	−0.6 (6.7)	−0.1 (8.3)	0.4 (8.8)	2.6 (44.0)	1.1 (0.5)	0.78	719

In each set of numbers the first is the mean, and the number in parentheses is the standard deviation. V is vertically polarized, and H is horizontally polarized.

encompasses the entire Arctic Basin, which we sample at 3-day intervals. The second region covers Fram Strait and Baffin Bay on the east and west coasts of Greenland. The last region is the Weddell Sea. The ice motion in the latter two regions are characterized by large ice displacements and deformation with active ice growth/ablation in the winter. We use a 1-day sampling period in these regions. Examples of the 1- and 3-day 85-GHz displacement fields from these regions are shown in Figures 1, 2, and 3. Note that the density of observations obtained is still quite high after the filtering process. For comparison, buoy displacement vectors are shown along with the observed displacement vectors. The agreement between the displacement observations is quite remarkable; quantitative evaluation of these fields is provided in the next section. Overlay of the surface pressure field over the derived motion field also shows the circulation pattern to be generally tangent to the isobars. We note here that all the vectors in the motion field were generated by the tracking process, and no attempt was made to fill in these holes by interpolation; there are grid points where the tracker did not provide a motion observation.

3. Error Analysis

In order to quantify the uncertainties in the ice motion from passive microwave data and to understand the utility of these measurements, we compare the motion results with those derived from drifting buoys and the analysis of sequential SAR images. Motion information from buoys, available at 3-hour intervals are used for comparison purposes because the higher sampling rate allows us to better match the observation times of the passive microwave data set without resorting to temporal interpolation of the position measurements. SAR-derived ice motion is used in areas where no or few buoys are available. This comparison study is done with SSM/I motion results from the Arctic and Antarctic winters of 1992 and 1993. We also compare the ice motion results obtained using the 37-GHz and the 85-GHz channel data sets. The results show that we can reliably obtain ice motion, albeit at a slightly higher level of uncertainty, from the 37-GHz brightness temperature fields. The three regions used in our analysis, described in the previous section, have been selected because they have different motion characteristics and buoy and SAR motions are available for comparisons.

3.1. Source of SAR and Buoy Motion

The SAR ice motion data set used here is obtained by tracking common features in sequential ERS-1 radar imagery using a tracking approach similar to the one described here. We compiled SAR motion measurements from two regions of the Arctic: Beaufort Sea and Fram Strait. The gridded SAR ice motion data from the Beaufort Sea are produced by the Geophysical Processor System [*Kwok et al.*, 1990] at the Alaska SAR Facility. The ERS SAR motions are typically produced from images separated by 3 days. In total, 200 3-day displacement fields on a 5-km grid covering an area of ~100 × 100 km were available during this period. The Alaska SAR Facility reception mask, however, does not cover the Fram Strait region, and no equivalent facility providing ice motion processing exists for data outside its coverage area.

SAR ice motions for the Fram Strait region are computed from images obtained from the European Space Agency. Low-resolution quicklook images and high-resolution image products were reformatted to allow the computation of displacements by a copy of the Geophysical Processor System located at the Jet Propulsion Laboratory. Displacement errors are estimated to be <300 m. Approximately 1000 image pairs at time intervals varying from 1 to 7 days are obtained for this region. However, the whole data set is not used here because some motion pairs did not have suitable start times or correct time separations between observations.

Buoy data are obtained from two different sources. Arctic data were provided by the International Arctic Buoy Program (IABP). The buoy positions at 3-hour intervals are interpolated from positions sampled at 1–2-hour intervals by fitting a polynomial to the time series data. The position accuracy is estimated to be ≈350 m [*Thorndike and Colony*, 1980]. Buoy data for the Weddell Sea were collected and preprocessed by the Alfred Wegener Institute (AWI). Some of the buoys are equipped with Global Positioning System (GPS) receivers. Errors in positions are ~350 m for the buoys using the ARGOS positioning system and better than 50 m for those using the GPS system [*Kottmeier et al.*, 1992].

3.2. Comparison With Buoy/SAR Ice Motion

Though spatially sparse, ice motions from the IABP buoys are the best measurements for assessing the quality of passive microwave motion because of its continuous temporal cover-

Table 3. Comparison of 37-GHz Ice Motion With Buoy Motion for October 1992 to May 1993

Region	Channel, GHz	Interval, days	Δ, km	e_x, km	e_y, km	θ, km	Scale	ρ	Number of Points
			All Points						
Arctic	37 V	3	−0.4 (10.6)	3.7 (8.7)	0.2 (9.2)	−2.7 (49.1)	4.4 (19.8)	0.79	2242
	37 H	3	0.6 (11.3)	3.7 (9.8)	0.5 (10.1)	−1.9 (51.6)	4.4 (22.1)	0.77	2181
Fram Strait/Baffin Bay	37 V	1	−1.7 (7.6)	1.5 (5.1)	2.1 (6.9)	−2.1 (61.4)	2.5 (6.2)	0.61	590
	37 H	1	−1.9 (8.1)	1.4 (5.3)	2.4 (7.1)	3.4 (62.5)	2.7 (6.0)	0.57	573
			Excluding Points With Small Displacements						
Arctic	37 V	3	−0.3 (7.0)	3.7 (7.9)	−0.4 (7.6)	−0.8 (25.2)	1.0 (0.3)	0.89	842
	37 H	3	0.2 (7.7)	3.5 (8.7)	0.0 (8.5)	−0.3 (28.2)	1.1 (0.4)	0.87	853
Fram Strait/Baffin Bay	37 V	1	−0.2 (5.5)	1.2 (5.6)	0.2 (5.8)	−2.0 (34.9)	1.1 (0.5)	0.77	105
	37 H	1	0.0 (5.2)	0.7 (5.5)	0.3 (5.7)	2.0 (36.3)	1.1 (0.5)	0.78	106

In each set of numbers the first is the mean, and the number in parentheses is the standard deviation.

age. To date, SAR-derived ice motions are dependent on available reception facilities, and satellite coverage of the Arctic and Antarctic are limited to certain regions and seasons. Results from the comparison of 8 months of Arctic and Antarctic SSM/I ice motions with buoy and SAR ice motions are shown in Tables 2, 3, and 4. Scatterplots of the passive microwave and buoy motions are shown in Figures 4 and 5. In Tables 2–4 we measure the quality of the displacement estimates with the following quantities:

$$\mathbf{e} = \mathbf{u}_{SSM/I} - \mathbf{u}_{ref}$$

$$\Delta = |\mathbf{u}_{SSM/I}| - |\mathbf{u}_{ref}|$$

$$\theta = \arccos \frac{\mathbf{u}_{SSM/I} \cdot \mathbf{u}_{ref}}{|\mathbf{u}_{SSM/I}||\mathbf{u}_{ref}|}$$

$$\rho = \frac{\sum \mathbf{u}_{SSM/I} \cdot \mathbf{u}_{ref}}{\sum |\mathbf{u}_{SSM/I}||\mathbf{u}_{ref}|}$$

$$scale = |\mathbf{u}_{SSM/I}|/|\mathbf{u}_{ref}|$$

where **e** is the vector difference between $\mathbf{u}_{SSM/I}$ and $\mathbf{u}_{ref}$, where ref denotes either buoy or SAR motion data. Here e_x and e_y are the components of **e** in the two orthogonal directions defined by the SSM/I polar stereographic map projection; the abscissa and ordinate are defined by the 45° and 135°E meridians, respectively. The angular or directional difference between the two vectors is θ; ρ is the correlation between two displacement data sets, and scale is the ratio of the displacement magnitudes of the motion estimates. The standard deviations of the differences in each case are measures of uncer-

tainty in the derived displacement vectors. Each quantity measures a different aspect of the displacement estimates.

The dominant sources of error in the measurement of motion are errors in geolocation of the pixels, σ_g (standard deviation); location errors due to binning of the data, σ_b; and errors in ice motion tracking, σ_f. Assuming that the errors are normally distributed, unbiased, and uncorrelated, the expected errors in the displacement estimates, σ_u, are given by [Holt et al., 1992]

$$\sigma_u^2 = 2(\sigma_g^2 + \sigma_b^2) + \sigma_f^2$$

The expected magnitude of these and other errors are shown in Table 5. Using these values, σ_u is then ~16 and 25 km for the 85- and 37-GHz motion estimates, respectively. If any of these errors are correlated, the displacement uncertainties would be reduced. We also note a shortcoming of the input data used in motion tracking. Errors in the motion estimates are introduced by the manner in which current gridded brightness temperature data sets are constructed; ascending and descending observations at different times are binned and averaged to create the gridded field. Brightness temperatures observed over a 24-hour period (midnight to midnight UT) are summed then divided by the total number of observations to obtain an average brightness temperature at a pixel. So features are spatially distorted, and these fields of pixels are not associated with a distinct instant in time. This creates a spatial and temporal smearing or blurring of the brightness temperature fields, which is dependent on the magnitude of the local ice motion. Accounting for the contribution these factors, we

Table 4. Comparison of SSM/I Ice Motion with SAR Motion for October 1992 to May 1993

Region	Channel, GHz	Interval, days	Δ, km	e_x, km	e_y, km	θ, km	Scale	ρ	Number of Points
			All Points						
Arctic	85	3	−0.9 (7.3)	1.9 (11.1)	−0.8 (7.1)	1.2 (44.2)	1.5 (3.7)	0.74	108
	37	3	0.0 (7.3)	4.0 (12.3)	−2.0 (7.7)	3.6 (46.9)	1.3 (2.0)	0.75	122
Fram Strait/Baffin Bay	85	1	0.3 (4.8)	−0.2 (4.7)	0.2 (5.5)	−2.8 (43.0)	1.1 (0.6)	0.84	105
	37	1	0.1 (5.3)	−0.1 (3.9)	0.6 (6.4)	−0.7 (50.2)	1.2 (0.7)	0.82	92
			Excluding Points With Small Displacements						
Arctic	85	3	−1.8 (6.1)	1.9 (5.9)	−1.2 (6.1)	2.5 (15.3)	1.0 (0.3)	0.93	81
	37	3	−0.3 (6.4)	4.0 (6.1)	−2.1 (6.5)	3.9 (18.1)	1.0 (0.3)	0.92	68
Fram Strait/Baffin Bay	85	1	0.8 (3.9)	0.1 (3.7)	−0.1 (5.0)	−6.0 (25.9)	1.1 (0.4)	0.86	45
	37	1	0.5 (3.4)	−0.0 (2.7)	−0.1 (5.4)	−7.3 (24.3)	1.1 (0.3)	0.87	39

In each set of numbers the first is the mean, and the number in parentheses is the standard deviation.
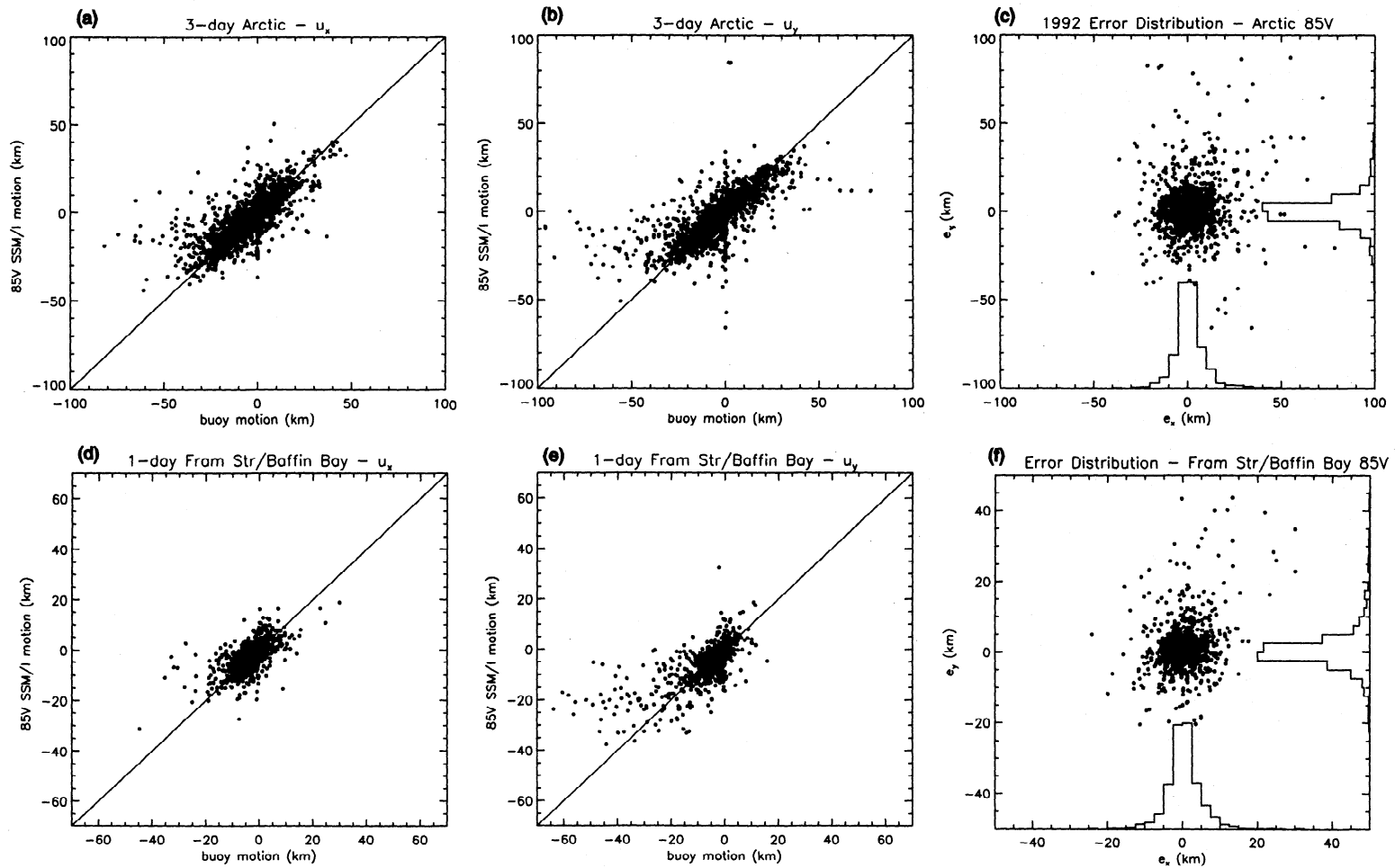
Figure 4. Comparison of the 85-GHz ice motion with buoy displacements. Scatterplot of u_x, u_y and error distributions e_x, e_y. Here e_x and e_y are the components of $\mathbf{e}(=\mathbf{u}_{SSM/I} - \mathbf{u}_{buoy})$ in the two orthogonal directions defined by the special sensor microwave/imager (SSM/I) polar stereographic map projection. (a) Scatterplot of $u_x^{SSM/I}$ versus u_x^{buoy} (3-day Arctic), (b) scatterplot of $u_y^{SSM/I}$ versus u_y^{buoy} (3-day Arctic), (c) plot of e_x versus e_y (3-day Arctic), (d) scatterplot of $u_x^{SSM/I}$ versus u_x^{buoy} (1-day Fram Strait/Baffin Bay), (e) scatterplot of $u_y^{SSM/I}$ versus u_y^{buoy} (1-day Fram Strait/Baffin Bay), (f) plot of e_x versus e_y (1-day Fram Strait/Baffin Bay), (g) scatterplot of $u_x^{SSM/I}$ versus u_x^{buoy} (1-day Weddell Sea), (h) scatterplot of $u_y^{SSM/I}$ versus u_y^{buoy} (1-day Weddell Sea), and (i) plot of e_x versus e_y (1-day Weddell Sea).
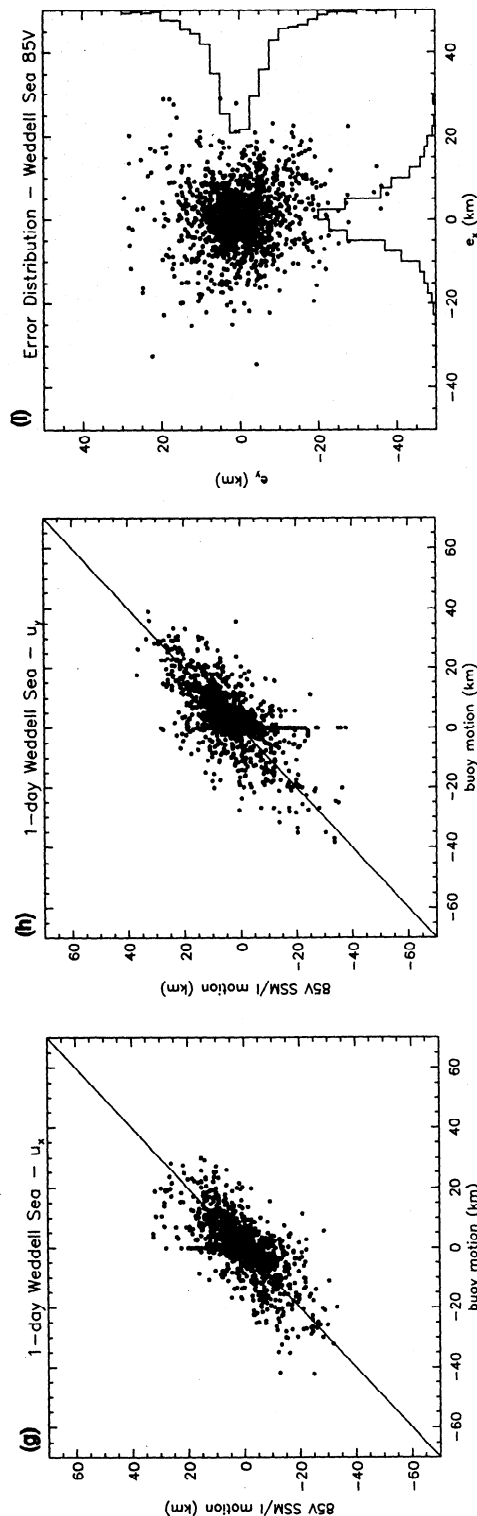
Figure 4. (continued)

expect displacement errors observed here to be larger than our estimate of σ_u above.

Here our measurement process also contributes additional uncertainties to the observation of σ_u. Since we use buoy/SAR displacements as truth, errors in these quantities add to the uncertainty of σ_u. However, the errors in the SAR and buoy ice motions by themselves are relatively insignificant compared to the sensor resolution, location, and tracking errors. There are measurement errors, however, due to the spatial and temporal misregistration of the passive microwave displacement vectors and the buoy/SAR motions. In our comparison we select grid points that are spatially (within 40 km) and temporally closest to available buoy/SAR observations for comparisons. We do not spatially or temporally interpolate the data sets to colocate the observations. Hence the measurements could be up to 12 hours (see discussion above) out of phase in time and/or separated by a distance of 40 km. Any temporal misregistration introduces variability into the comparison especially since sea ice motion on the average decorrelates fairly quickly with time, 1 day [*Thorndike*, 1984]. Variability could also be caused by the difference between the meaning of displacement between SSM/I motion measurements and buoy/SAR measurements. Motion derived from the passive microwave data are areal averages of displacements over the array of points ($\sim$100 $\times$ 100 km and 200 $\times$ 200 km in the 85- and 37-GHz data, respectively) used in the tracking procedure while buoy displacements are computed using sequential point position measurements on the ice cover. We choose not to interpolate the passive microwave motion to the buoy locations because the observations already represent the mean motion over a large area on the ice cover. Decorrelation of the buoy measurements and passive microwave measurements is expected if there are large local velocity gradients. Altogether, the measurement of σ_u is contaminated by the errors discussed here.

The results in Tables 2, 3, and 4 indicate that the magnitude of the uncertainties in displacement are slightly better than that computed above. As given in Tables 2 and 3, the standard errors are 13 km for Arctic Ocean, 7 km for Fram Strait, and 9 km for the Weddell Sea. The distribution of errors (Figure 4i) from the Weddell Sea results seem to have a larger scatter because some of the buoys near the coast were motionless at certain times during the season (see Figure 3) and atmospheric contamination may be more of a problem in the Weddell Sea. We also note that there are latitudinal differences between the gridded fields used in the motion tracking; in the Arctic most of the ice cover is above 70°N, and in the Antarctic most of the ice cover is north of 70°S. The number of pixels used to compute an average brightness temperature is smaller in the lower latitudes because of the divergence of the orbits; there are more missing passive microwave pixels in the Weddell Sea fields compared to the Arctic Ocean.

The small biases in e_x and e_y are discussed later in this section. The directional errors between the passive microwave ice motion and the buoy/SAR displacement vectors are small and unbiased. However, the average ratios of the displacement magnitudes (scale) of the measurements, which in the absense of noise we expect to be unity, seem unreasonably large. In the derived motion field we expect subresolution scale displacements to be noisy and would give large "scale" errors, i.e., the division of two numbers with low signal content. The mean scale is greater than unity because of the larger uncertainty of the passive microwave measurements in the numerator. Here
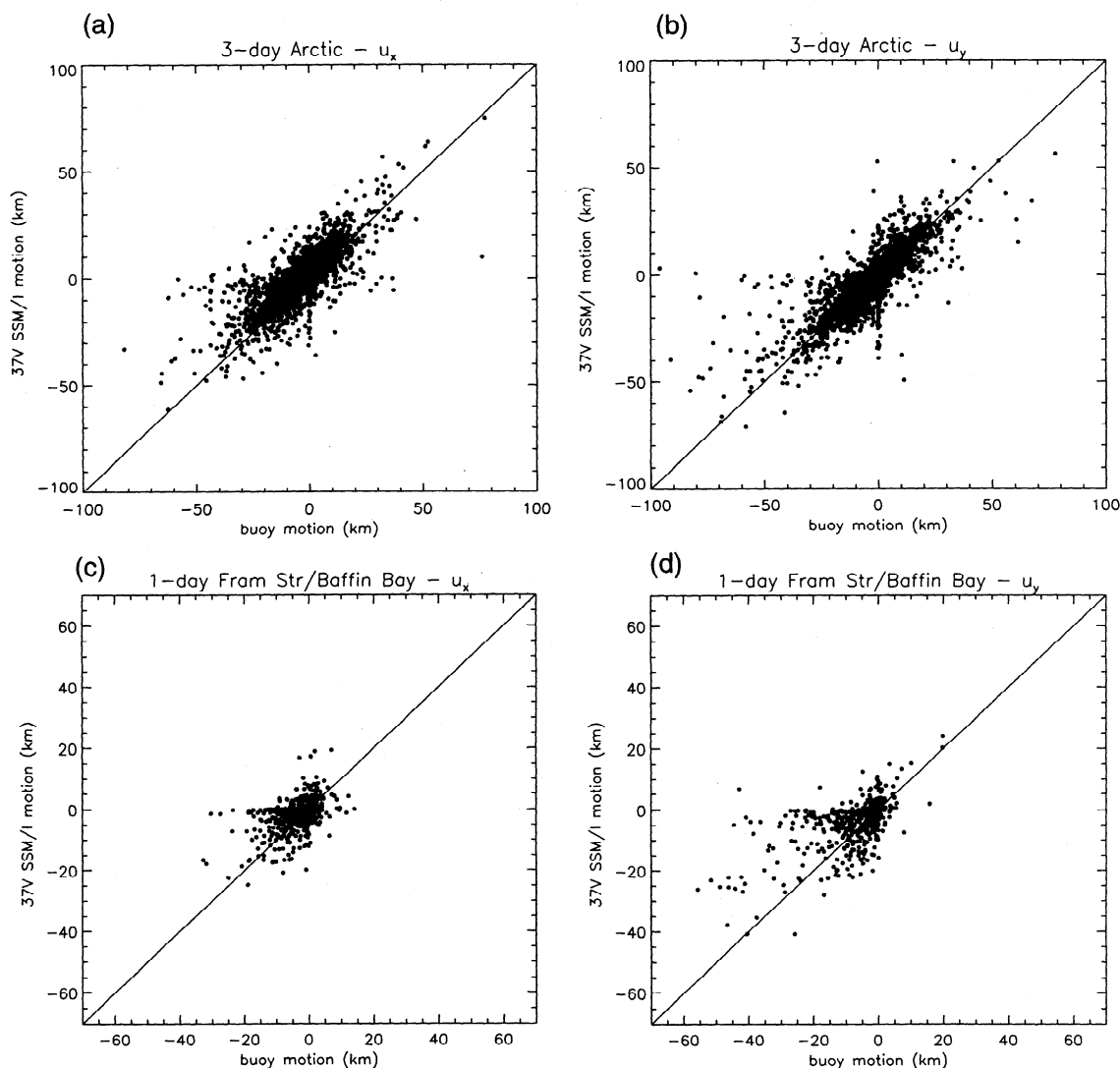
Figure 5. Comparison of the 37-GHz ice motion with buoy displacements. (a) Scatterplot of $u_x^{SSM/I}$ versus u_x^{buoy} (3-day Arctic), (b) scatterplot of $u_y^{SSM/I}$ versus u_y^{buoy} (3-day Arctic), (c) scatterplot of $u_x^{SSM/I}$ versus u_x^{buoy} (1-day Fram Strait/Baffin Bay), and (d) scatterplot of $u_y^{SSM/I}$ versus u_y^{buoy} (1-day Fram Strait/Baffin Bay).

the uncertainty of the quantity in the numerator is on the order of 5–10 km while the uncertainty of the denominator is ~350 m, a difference of more than an order of magnitude. To examine the contribution of noisy vectors to the comparisons, we excluded all data points where the displacements were less than half the pixel spacing (6.25 km for 85-GHz data and 12.5

Table 5. Sources of Displacement Errors

Source	Expected σ
Geolocation error (σ_g) [*Goodberlet*, 1990], km	8
SSM/I binning error (σ_b)	0.5 pixel spacing
Tracking error (σ_f)	≈0.5 resolution element
Buoy motion (ARGOS/GPS), m	350/50
SAR motion (ERS), m	300
Misregistration between SSM/I and buoy/SAR ice motion	see text
Temporal smearing of brightness temperature field	see text

The expected σ is standard deviation.

km for 37-GHz data) and recomputed the statistics. More points are excluded from the 37-GHz results. This choice of threshold is not based on the data; rather, the expected error in the displacement estimates is from the tracker. The results in Tables 2, 3, and 4 show mean scale values close to unity as well as a decrease in the variability in the directional differences between the measurements. The decrease in the number of points used, after we excluded the points with small displacements, indicates the number of observations with motion which are less than the above thresholds. These results illustrate quite well the limitations of the observations; when the motions are small compared to the spatial resolution of the data, the displacements are noisy because they are comparable to the noise amplitude. We do not suggest the deletion of small displacement vectors from motion fields because the noise contribution to individual estimates would be reduced (averaging process) in the creation of mean fields of motion.

It is also remarkable that the uncertainty in the 37-GHz motion (in Table 3) is only slightly worse than the 85-GHz estimates, even though the spatial resolution is approximately
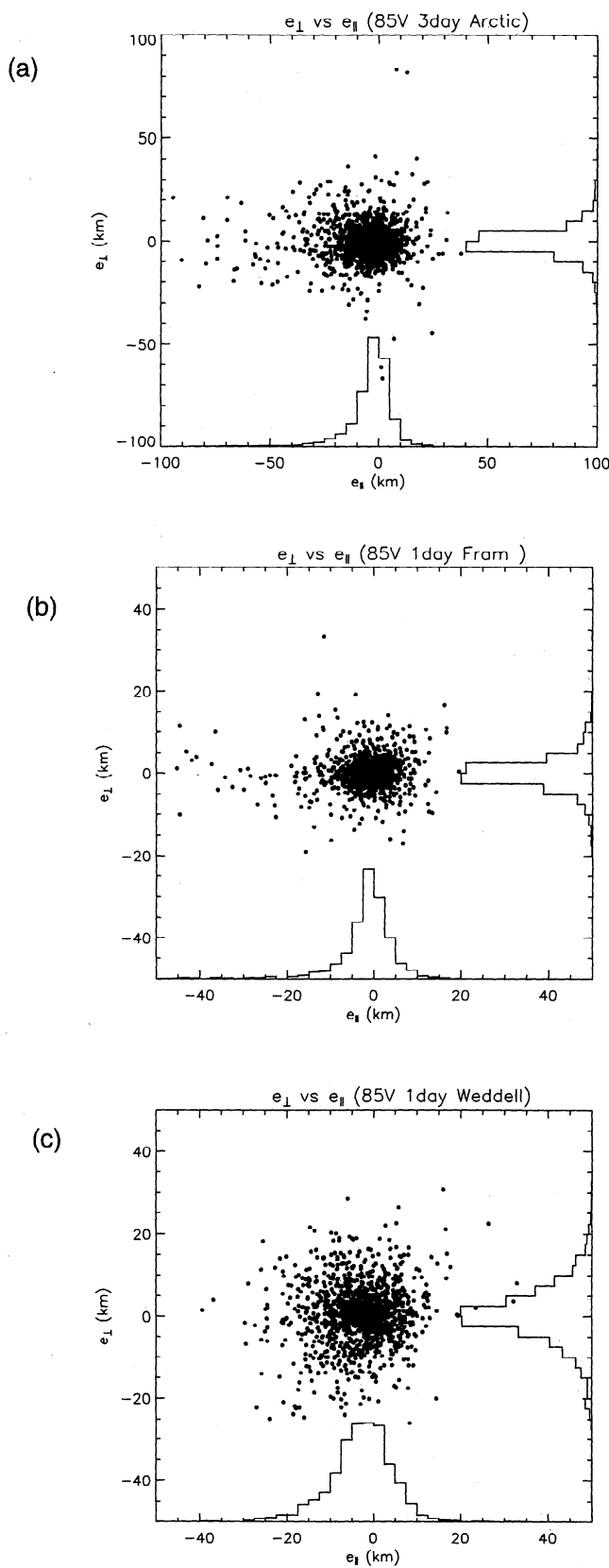
Figure 6. Plot of the displacement errors in the directions perpendicular, $e_\perp(=u_\perp)$, and parallel, $e_\parallel(=u_\parallel - |\mathbf{u}_{buoy}|)$, to the direction of buoy motion; (a) 3-day Arctic, (b) 1-day Fram Strait/Baffin Bay, and (c) 1-day Weddell Sea.
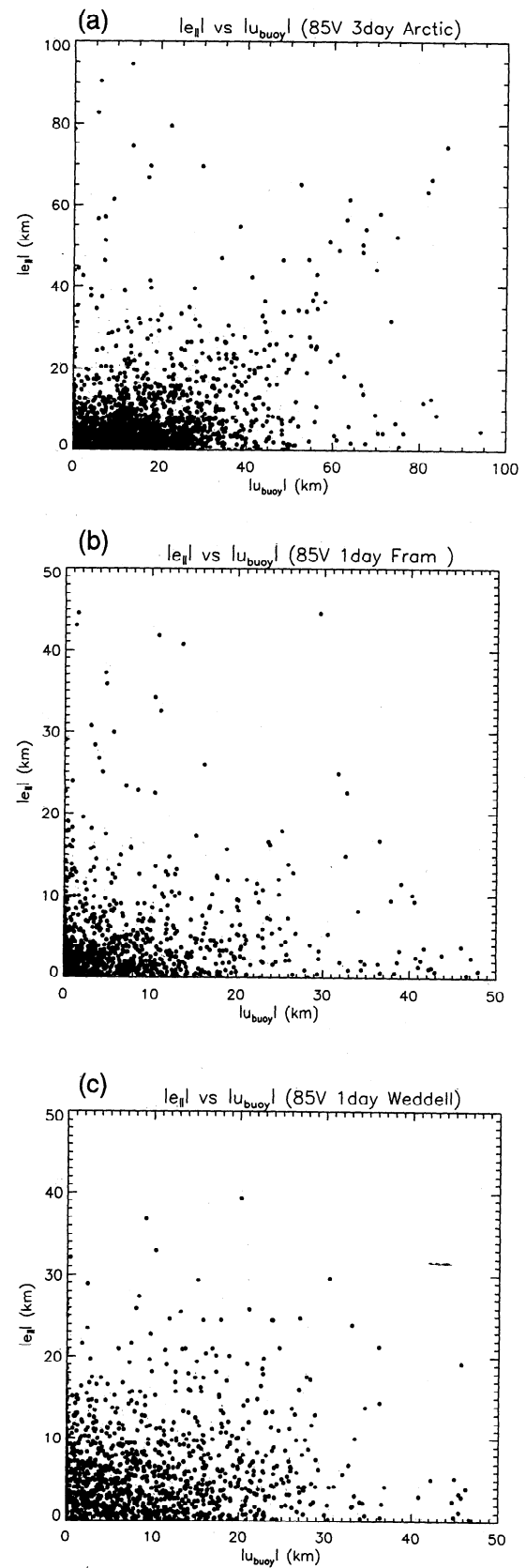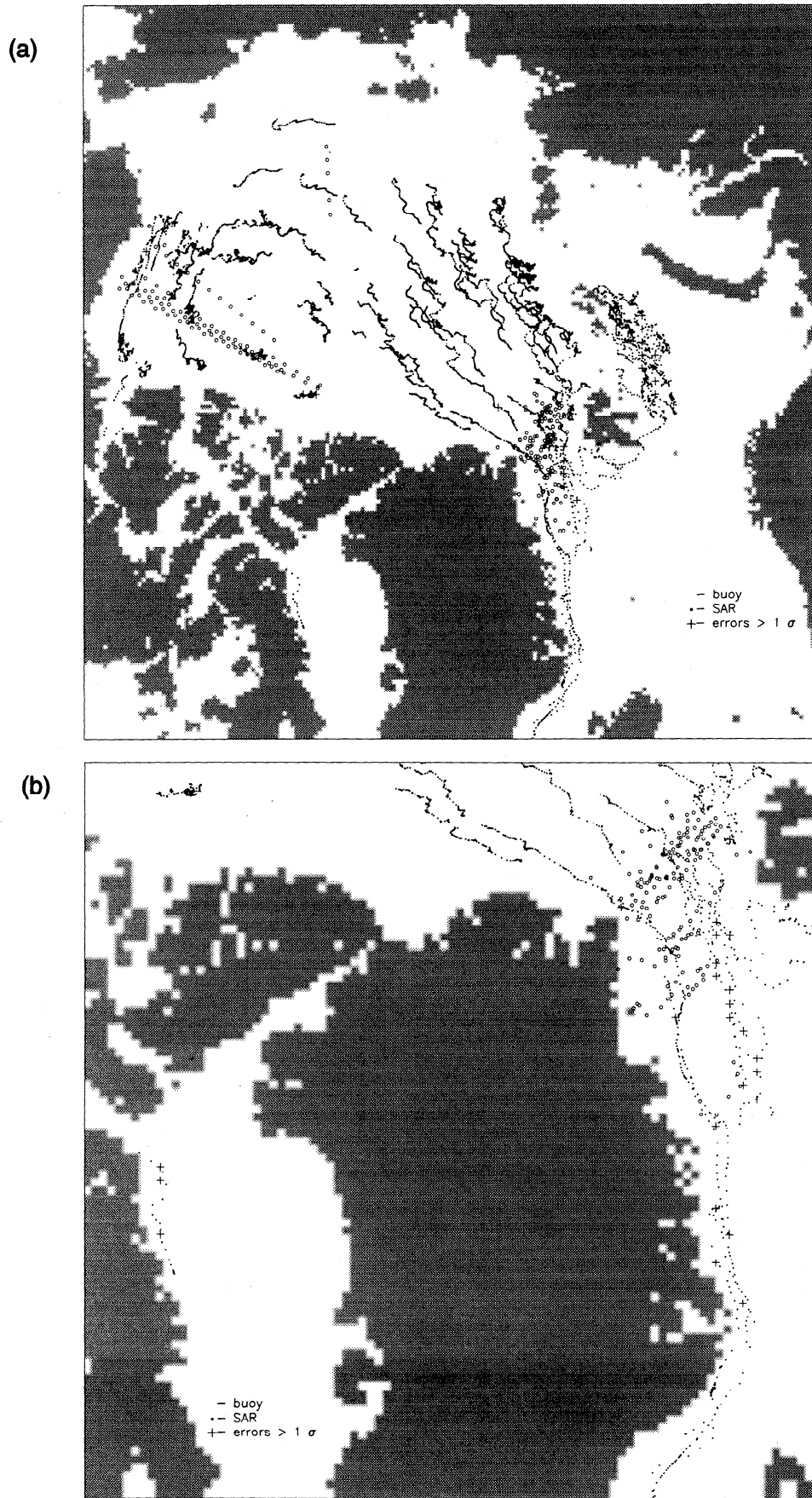
Figure 7. Plot of the displacement errors in the directions perpendicular, $e_\perp(=u_\perp)$, and parallel, $e_\parallel(=u_\parallel - |\mathbf{u}_{buoy}|)$, to the direction of buoy motion; (a) 3-day Arctic, (b) 1-day Fram Strait/Baffin Bay, and (c) 1-day Weddell Sea.

Figure 8. Location of the passive microwave ice motion estimates with errors >1σ (crosses) from the mean; (a) Arctic, (b) Fram Strait/Baffin Bay, and (c) Weddell Sea. Buoy positions (dots) and locations where SAR ice motion are available (open circles) are also shown.
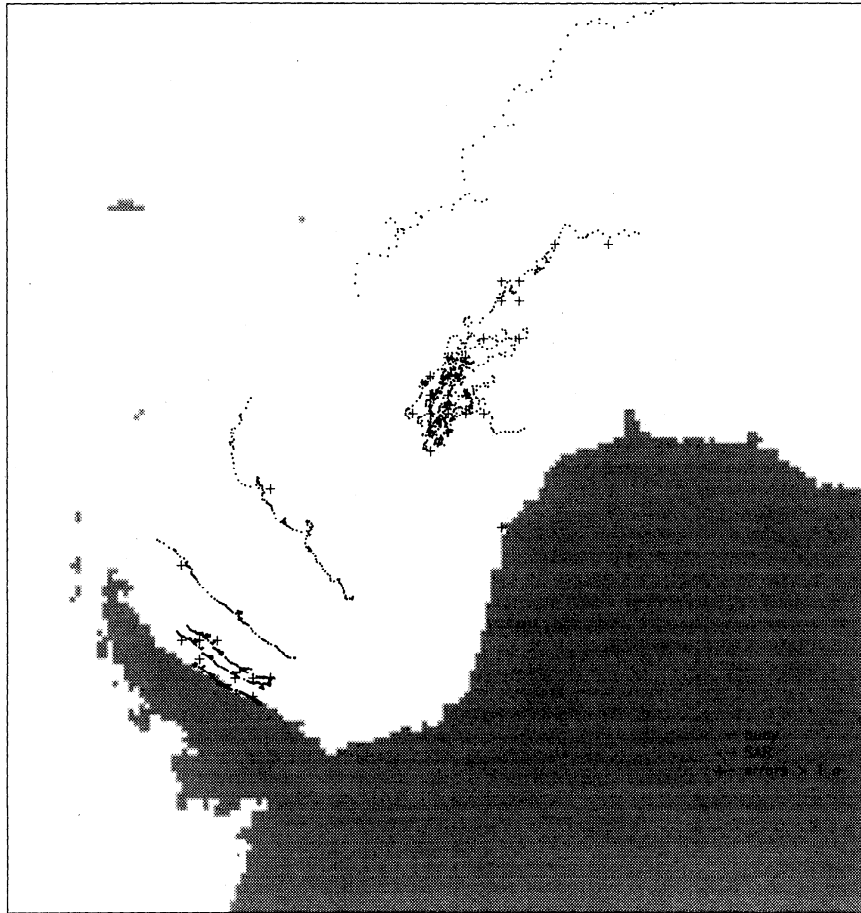
(c)

Figure 8. (continued)

twice as coarse. At 37 GHz the tracker uses a brightness temperature field 4 times the area as that of the 85-GHz data (200 × 200 km instead of 100 × 100 km). This additional area could be significant in determination of the average location or offset using the cross-correlation technique. We also note that the 37-GHz signal is relatively unaffected by atmospheric noise, such that the resolution advantage of 85-GHz could be partly offset by its sensitivity to atmospheric emissions.

Table 4 shows results of the comparison between 37- and 85-GHz ice motion and SAR ice motion. Each SAR ice motion observation represents the average ice motion over a ERS-1 100- × 100-km image frame. As discussed above, this may be a more compatible comparison as the passive microwave motion also measures spatially averaged motion rather than the motion of discrete particles on the ice cover. Indeed, the results indicate, albeit with a smaller number of points available, that the passive microwave motion compares more favorably with SAR ice motion than the buoy ice motion. The average correlation between the motion estimates are higher and the directional differences are lower than results from the comparisons between passive microwave motion and buoy motion. The uncertainty and biases in the displacements are, however, similar to the buoy comparisons.

Of greater concern are the biases in the displacement estimates shown in Tables 2, 3, and 4. These statistically significant biases (highest in the Arctic, 1 km), although quite small in comparison to the resolution of the sensors, are similar when compared to buoy and SAR ice motions. In Figures 4 and 5 we

see that the distribution of errors, e_x versus e_y, appear to be isotropic; that is, they have no particular orientation in space. Figure 6, however, shows that there is structure when the errors are projected in directions which are parallel ($e_{\parallel} = u_{\parallel} - |u_{buoy}|$) and perpendicular ($e_{\perp} = u_{\perp}$) to the direction of buoy motion. Here we have taken u_{buoy} to be our best estimate of the true displacement and u to be the SSM/I displacement. The $e_{\parallel}$ versus $e_{\perp}$ plots clearly indicate that the biases are introduced by errors which are in the direction parallel to the motion rather than perpendicular to it. Hence this noise process did not manifest itself as directional biases in the comparison statistics. The orientations of these biases are not resolved in the e_x versus e_y plots because the average ice motion over a large region like the Arctic typically has no clear directional preference. The mean error of the population, $e_{\parallel}$, seems to be biased by a small sample population of SSM/I motion observations, which underestimated the actual motion as evidenced by the tail of the histogram. Figure 7 shows the dependence of the errors on the magnitude of motion. There seems to be a small dependence of the 3-day Arctic SSM/I motion estimates on the magnitude of displacement (Figure 7a), although this dependence is not obvious in the 1-day Fram Strait/Baffin Bay and Weddell Sea motion estimates. Next, we examine the spatial location of the points with errors $>1\sigma$ of the uncertainty shown in Tables 2 and 3. When we first mapped these erroneous vectors, we thought they must be associated with a shear zone near Greenland and near the ice edge, but Figure 8 shows that the locations of the errors are determined simply
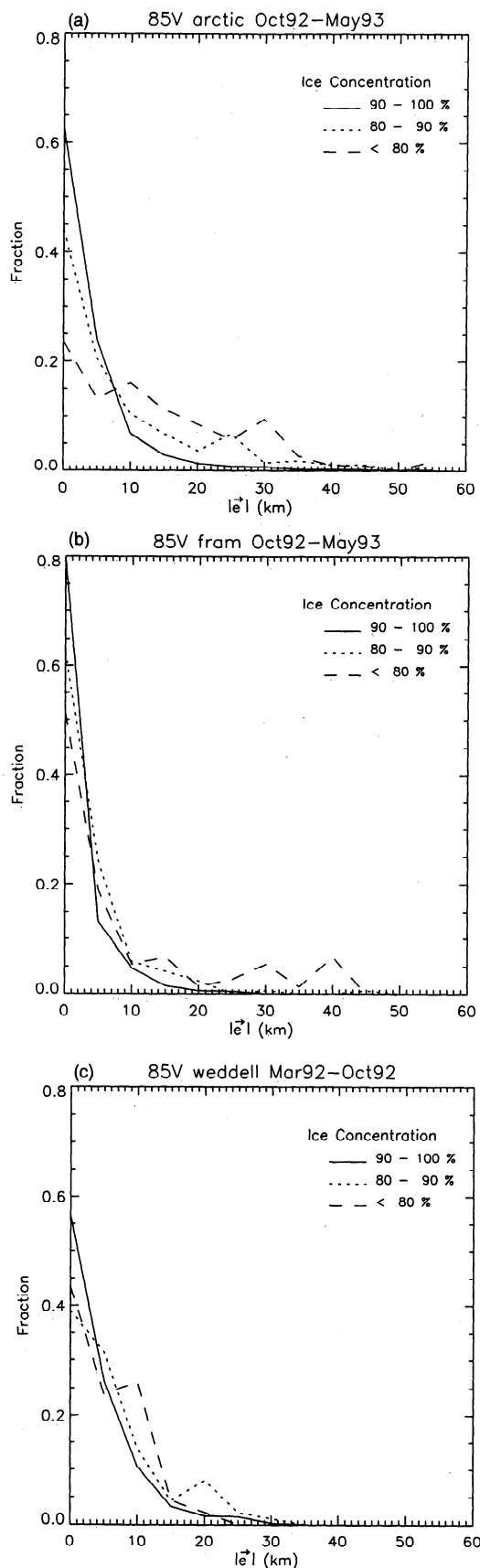
Figure 9. Histograms showing the error distribution as a function of three ranges of ice concentrations: (a) Arctic, (b) Fram Strait/Baffin Bay, and (c) Weddell Sea.

by where corroborative buoy tracks are located. Figure 8a, however, shows that the least reliable tracking occurs in the first-year ice of the Barents and eastern Arctic Ocean, where the motion is dynamic and where the brightness temperature fields are affected by storm systems that are active in this region. Tracking in the central Arctic seems more reliable. The regions with the least reliable results are also areas with typically lower ice concentration. In Figure 9 we plot the distribution of errors at different ranges of ice concentration. In the Arctic Ocean we find that the error distributions are broader as the ice concentration decreases; in other regions the effect does not seem to be as strong. In areas of lower ice concentrations it is possible that the ice motion from drifting buoys are less representative of the area-averaged ice motion obtained from SSM/I. This hypothesis (also suggested by *Kottmeier et al.* [1992]), however, cannot be easily tested with available data sets. If, indeed, the ice concentration is a good indicator of larger uncertainty in the tracking, it could be used to further cull the SSM/I motion fields of unreliable estimates.

In summary we made the following observations about the error characteristics: larger errors seem to occur in conjunction with larger motion in the Arctic motion fields; this small population of large errors is not centrally distributed but skewed in such a way as to introduce small biases in the population mean; and the tracking results obtained in the certain regions and areas of lower ice concentration are generally less reliable. Why is the tracker output biased toward smaller ice motion estimates for large displacements? In regions with large displacements, large velocity gradients, or low ice concentration the spatial distribution of the brightness temperature in the fields used for tracking tends to decorrelate with time, thus reducing the likelihood of the tracker finding the correct offset. In such cases, where the brightness temperature field is indistinguishable from adjacent fields, an incorrect peak in the correlation surface could be located by the tracker. If this estimated offset satisfies all the criteria in the filtering process, it would be accepted and would be output as a displacement estimate. Typically, it is more difficult to remove erroneous estimates of smaller displacements because unreasonably large displacement errors are usually less coherent with the local fields of motion and inconsistent motion estimates are more easily discarded by the filtering process. The more effective filtering of erroneous large displacement estimates introduces a bias in the error statistics. Thus this could be caused by an asymmetry in the filtering of errors in the motion tracker. In any case the errors in the motion estimates are intimately dependent on the tracking and filtering processes. Some filters, which may effectively remove outliers, could inadvertently introduce biases in the measurements.

3.3. Comparison of Buoy- and SSM/I-Derived Trajectories

One helpful way to visualize the quality of the SSM/I-derived ice motion is to derive trajectories and compare them with buoy trajectories. Figure 10 shows the location of 16 buoy trajectories in the Arctic Ocean spanning the 8 months of our SSM/I motion data (October 1992 to May 1993). Both buoy and SSM/I trajectories are shown in Figures 11a–11p. To create an SSM/I ice trajectory, we start at the same time and location as that of a buoy. Subsequent locations of the SSM/I track are derived from the gridded 3-day SSM/I motion fields. A motion estimate at an arbitrary location is determined by interpolation using available grid points within a 50 km radius of that location. For each comparison (Figure 11) we show the
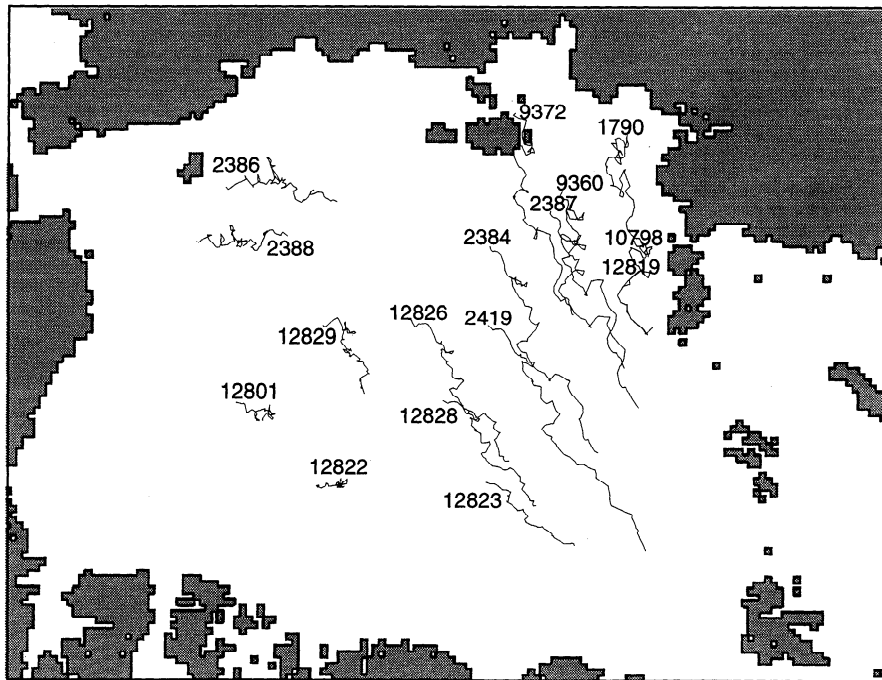
Buoy Tracks - Oct 92 through May 93

Figure 10. Location of buoy trajectories in the Arctic Ocean.

two trajectories and the corresponding differences in motion estimates during each 3-day period. Note that each plot has a different scale (shown in upper right-hand corner) that is dependent on the net displacement over the whole period. Locations where there were no SSM/I motion estimates (see Figures 11b and 11f) are indicated by zero differences between buoy and SSM/I displacements. In general, given the errors in the SSM/I motion estimates, the tracks agree reasonably well. If the errors were biased, we expect the derived tracks to diverge. The largest discrepancies are the tracks shown in Figures 11j, 11l, and 11p. These buoys (12801, 12822, 12829) are located in areas with relatively very little ice motion throughout the year (see scale on each plot). It is not surprising that these trajectories are noisy since these SSM/I motion estimates are dominated by noise. This suggests that maybe 6-day SSM/I ice motion fields should be considered or 3-day motion fields should be averaged to reduce the noise contribution in these slow-moving areas.

3.4. Polarization and Cross-Channel Comparisons

The vertically polarized (V) and horizontally polarized (H) channels at 85 and 37 GHz provide slightly different views of the ice cover as well as different sensitivities to atmospheric emissions (cloud liquid water, water vapor). In the winter Arc-

tic the ice cover could be modified by precipitation, storm systems, and opening/closing of leads. The presence of open water tends to decrease the brightness temperature observed by the H channel more than that of the V channel, although the contribution of open water to the total brightness temperature is probably rather small in the winter Arctic. Storm systems and precipitation could modify the passive microwave signature of the surface in a unpredictable ways. Ideally, for the purposes of ice tracking one would select the channel/ polarization which is least sensitive to the atmosphere and provides the highest contrast between surface features. The additional condition is that these surface features remain relatively stable over the period of observation. However, it is not clear at the outset whether there are any differences in the quality of the motion data obtained from the V or H channels. The comparison of the motion results from the H and V channels with buoy motion showed the uncertainties in the observed motion to be similar. Comparison of the motion of the H and V channels (shown in Table 6) shows that they are consistent and their errors are smaller than that when compared to buoys. In summary, there is relatively little difference between motion derived from the H and V channels.

Table 7 shows the consistency in the ice motion between 85

Table 6. Differences Between unfiltered Vertically and Horizontally Polarized Ice Motion for October 1992 to May 1993

Region	Channel, GHz	Interval, days	Δ, km	e_x, km	e_y, km	θ, km	Scale	ρ	Number of Points
Arctic	85	3	−0.4 (1.0)	−0.3 (1.2)	−0.2 (0.9)	0.2 (2.7)	1.1 (0.1)	0.87	46852
	37	3	−1.0 (1.4)	−0.3 (1.8)	−0.2 (1.9)	0.4 (3.5)	1.1 (0.1)	0.85	28325
Fram Strait/Baffin Bay	85	1	0.0 (0.7)	−0.1 (0.8)	−0.4 (0.8)	0.0 (3.9)	1.0 (0.1)	0.89	48933
	37	1	0.1 (2.3)	0.0 (2.7)	−0.3 (3.2)	−1.0 (10.9)	1.0 (0.1)	0.86	10871

In each set of numbers the first is the mean, and the number in parentheses is the standard deviation.
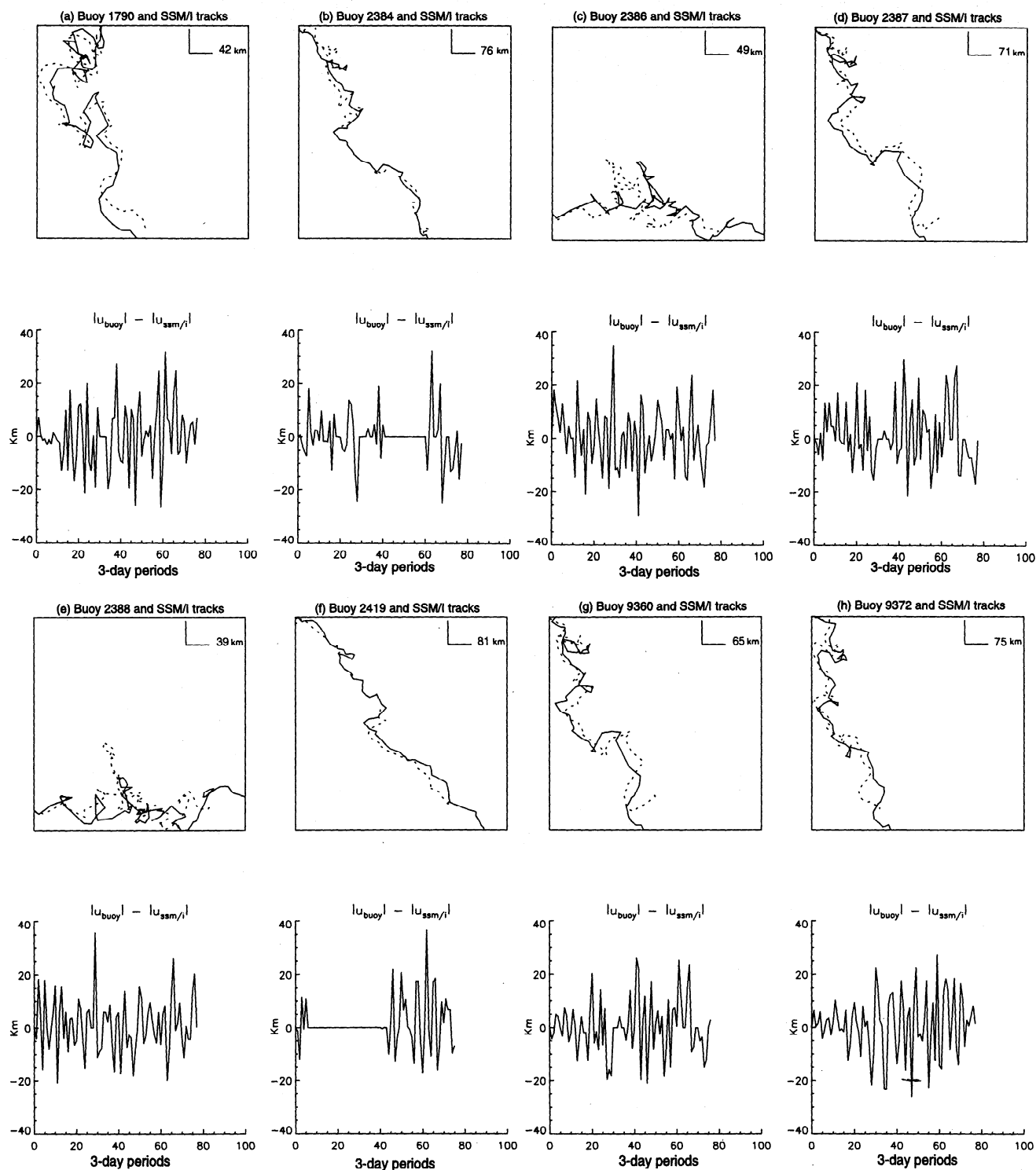
Figue 11. Comparison of 3-day buoy (solid line) and SSM/I derived (dashed line) tracks. (a) Buoy 1790, (b) buoy 2384, (c) buoy 2386, (d) buoy 2387, (e) buoy 2388, (f) buoy 2419, (g) buoy 9360, (f) buoy 9372, (i) buoy 10798, (j) buoy 12801, (k) buoy 12819, (l) buoy 12822, (m) buoy 12823 (n) buoy 12826, (o) buoy 12828, and (p) buoy 12829. Note scale on the top right-hand corner of each plot. c

and 37 GHz. Tables 2 and 3 already showed that there is only a slight degradation in the quality of the motion observations when one uses data from the lower-resolution channel. The biases in the observations between the two frequency channels are small. It is remarkable that the variance in the displacement estimates between the two channels are also small. This shows that it is feasible to obtain ice motion from the 37-GHz as well as the 85-GHz brightness temperature fields.
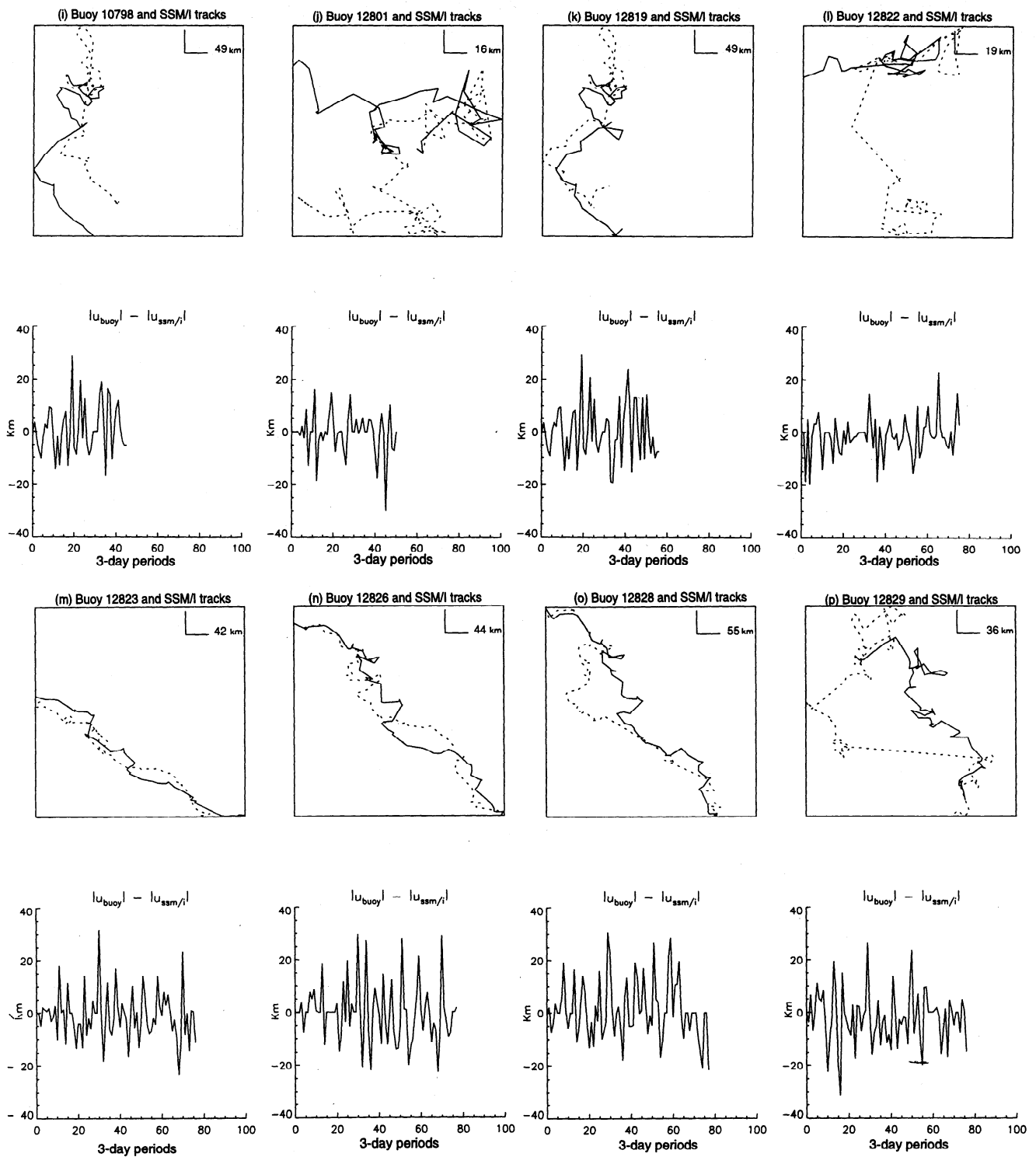
Figure 11. (continued)

4. Features in SSM/I Ice Motion Fields

We summarize the circulation patterns during the winter of 1992–1993 by grouping the Arctic passive microwave observations into fields of mean motion for October–November, December–January, February–March, and April–May and the Antarctic passive microwave observations into fields of mean motion for March–April, May–June, July–August, and September–October of 1993. The 2-month mean ice motion from the three regions is shown in Figures 12, 13, and 14. For the Arctic case we compare these mean fields with motion estimates using buoy and wind data; these fields were provided by the National Snow and Ice Data Center (NSIDC). The following subsection describes how the mean fields are computed from daily or 3-day motion fields. Then we describe the new perspective gained with the higher spatial detail of the motion fields.

Table 7. Differences Between SSM/I 37- and 85-GHz Horizontally or Vertically Polarized Ice Motion for October 1992 to May 1993

Region	Channel, GHz	Interval, days	Δ, km	e_x, km	e_y, km	θ, km	Scale	ρ	Number of Points
Arctic	85V-37V	3	−1.3 (2.0)	−3.4 (1.6)	−0.1 (2.0)	3.6 (6.2)	1.1 (0.1)	0.75	39603
	85H-37H	3	−1.9 (2.0)	−3.3 (1.6)	0.1 (1.5)	3.3 (6.7)	1.2 (0.1)	0.76	39329
Fram Strait/Baffin Bay	85V-37V	1	0.18 (1.7)	−1.6 (1.5)	−1.0 (1.9)	4.6 (9.3)	1.1 (0.1)	0.81	26186
	85H-37H	1	0.1 (1.6)	−1.2 (1.9)	−1.0 (1.8)	3.4 (10.6)	1.1 (0.1)	0.79	25731

In each set of numbers the first is the mean, and the number in parentheses is the standard deviation.

4.1. Creation of the Mean Motion Fields

The following procedure is used to fill in holes in the data before the averaging process. At grid points where the tracker did not provide any observations we use an interpolation procedure to provide a motion estimate. A displacement estimate at a point is created by normalized weighting of at least three observations within a 100-km neighborhood with their relative weights determined by a spatial autocorrelation function. We model this function with a decaying exponential, namely

$$R(x) = \exp\left(-\frac{|x|}{l}\right)$$

where l is a length scale derived for each motion field and x is the distance from the point of interest. We find that this functional form fits the data quite well, although the results are relatively insensitive to the shape of the autocorrelation function because in most cases the correlation of the measurements remains fairly high over a distance of 100 km. Sample correlation functions from the three regions are shown in Figure 15. We compute the data points in the following manner: At each point on our gridded motion field we compute the distance-dependent correlation of that point with other grid points within a radius of 600 km; the points on the plot represent the mean correlation values from the application of this procedure to all the grid points on the motion field. The length scales used in the interpolation of the motion fields are computed from the data itself. The variability of this parameter for the different regions over the winter period of 1992-1993 are 685 ± 332 km (Arctic Basin), 569 ± 365 km (Fram Strait/ Baffin Bay), and 875 ± 346 km (Weddell Sea).

The above procedure does not fill in all the holes in the data. There are remaining gaps in the time series of displacement vectors at a given grid point, because either there were no observations in the neighborhood for estimation of the motion or the sea ice concentration was <15% at that point. We compute an average displacement vector only if 80% of the observations are available over the 2-month period. For instance, the requirement is that there be at least 50 observations out of a maximum of 60 observations (1-day sampling) over a 2-month period before that grid point is included in the output field. Typically, this excludes points close to the ice edge as well as grid points in regions like Baffin Bay, where sea ice coverage remains low until late October (see Figure 13a).

4.2. Arctic Basin Circulation

Figures 12a, 12d, 12g, and 12j show the SSM/I-derived bimonthly mean fields of motion for the Arctic Basin between October 1992 and May 1993. The feature known as the Transpolar Drift is present, although its orientation and to a lesser extent its strength vary considerably. The other well-known feature of the long-term mean field, the Beaufort Gyre, is never fully formed in the bimonthly fields, although it is somewhat present in April and May of 1993. There is never significant flow parallel to the Canadian archipelago, whereas there are substantial westward flows along the Alaskan coast. The other major feature, the outflow through Fram Strait, can be seen to come from quite different parts of the ocean at different times; this would suggest that the ice thickness in the Fram Strait comes from a variety of source regions and could be quite variable. The February–March field shows a well-developed cyclonic circulation centered between the New Siberian Islands and Severnaya Zemlya. There is quite a significant alternating exchange between the Arctic Ocean and the Kara and Barents Seas. The Kara Sea appears to be a net exporter of ice, sometimes into the eastern Arctic Ocean and other times into the Barents Sea. The entire 8-month period shows flow out of the Laptev Sea, which is a primary source of ice in the Transpolar Drift stream. The New Siberian Sea is alternately a source or a sink of ice. Many of these features have never been observable in such spatial and temporal detail.

To put these fields into perspective, we compare these fields with ice motion fields obtained from interpolation of buoy observations coupled with estimates from a wind-driven ice drift model [Pfirman et al., 1997]. Early practice was to optimally interpolate a field of motion from about 10 to 20 buoy displacements, taking a "background" field of zero velocities. More recent practice has been to use geostrophic surface winds estimated from the gradient of surface pressure field as additional input to the motion interpolation. The correlation functions, used in the interpolation, have length scales of ~1500 km and represent motion on a large scale. At this length scale, smaller-scale structures in the motion field are smoothed. This scheme does not account well for the behavior of ice motion close to coasts or near islands in the Arctic, and the accuracy of these fields are dependent on the quality of the analyzed wind fields. Here we use fields interpolated from buoy and winds (provided by NSIDC) as the best source of motion estimates without satellite image tracking and compare these interpolated fields of motion with fields derived from SSM/I. The mean ice motion from the buoy fields and the differences between the passive microwave motion field and buoy-derived field are shown in Figures 12b, 12c, 12e, 12f, 12h, and 12i. The difference fields represent $u_{buoy/wind} - u_{SSM/I}$.

The October–November buoy/wind field (Figure 12a) shows an anomalous drift pattern in the southern Beaufort Sea compared to the SSM/I motions. This large eastward advection of ice near the coast is probably due to the existence of a high over the continent affecting the wind drift model. Also, a strong local anticyclonic motion pattern local to the Beaufort Sea can be observed. The SSM/I observed motion shows a very
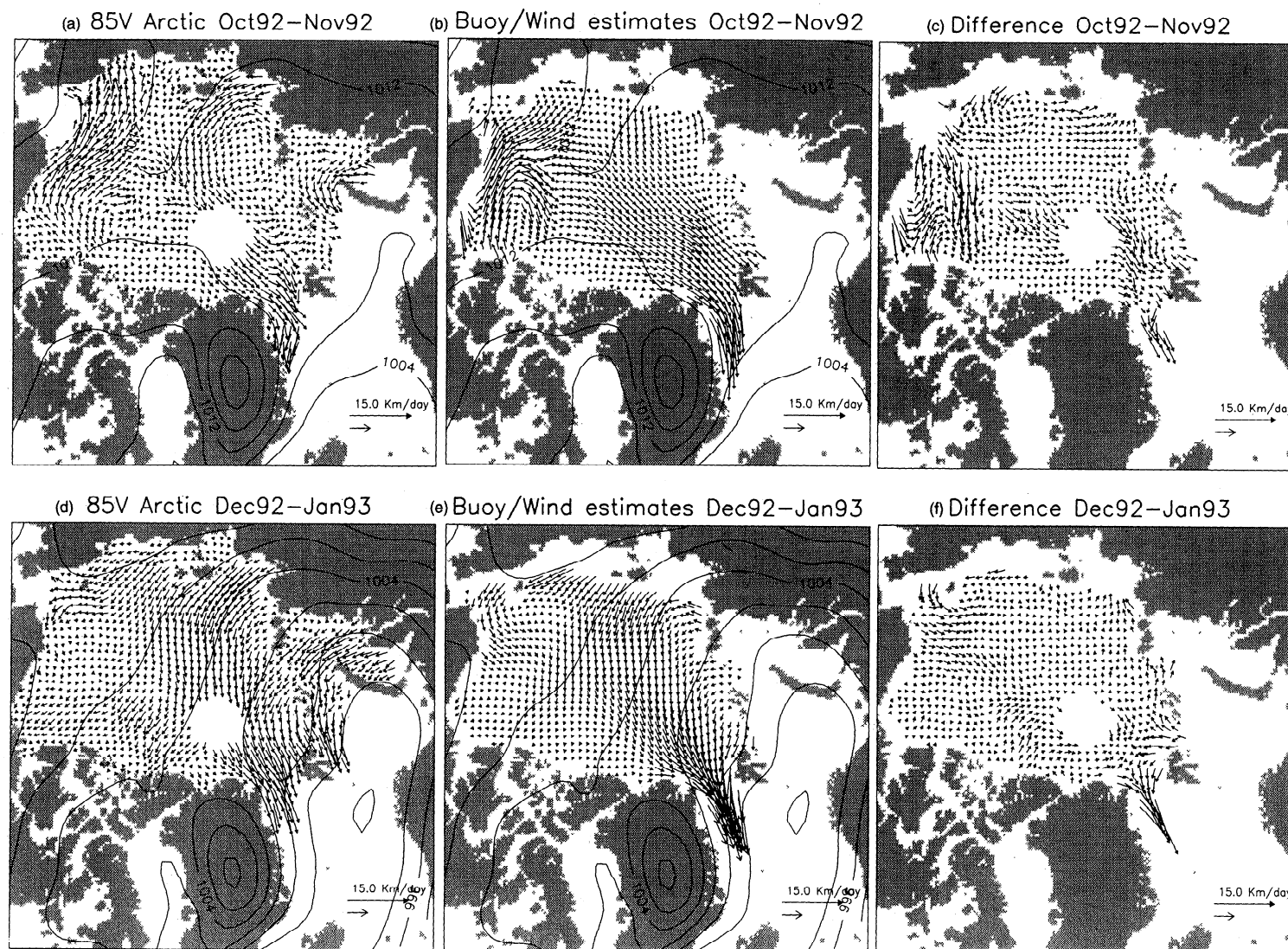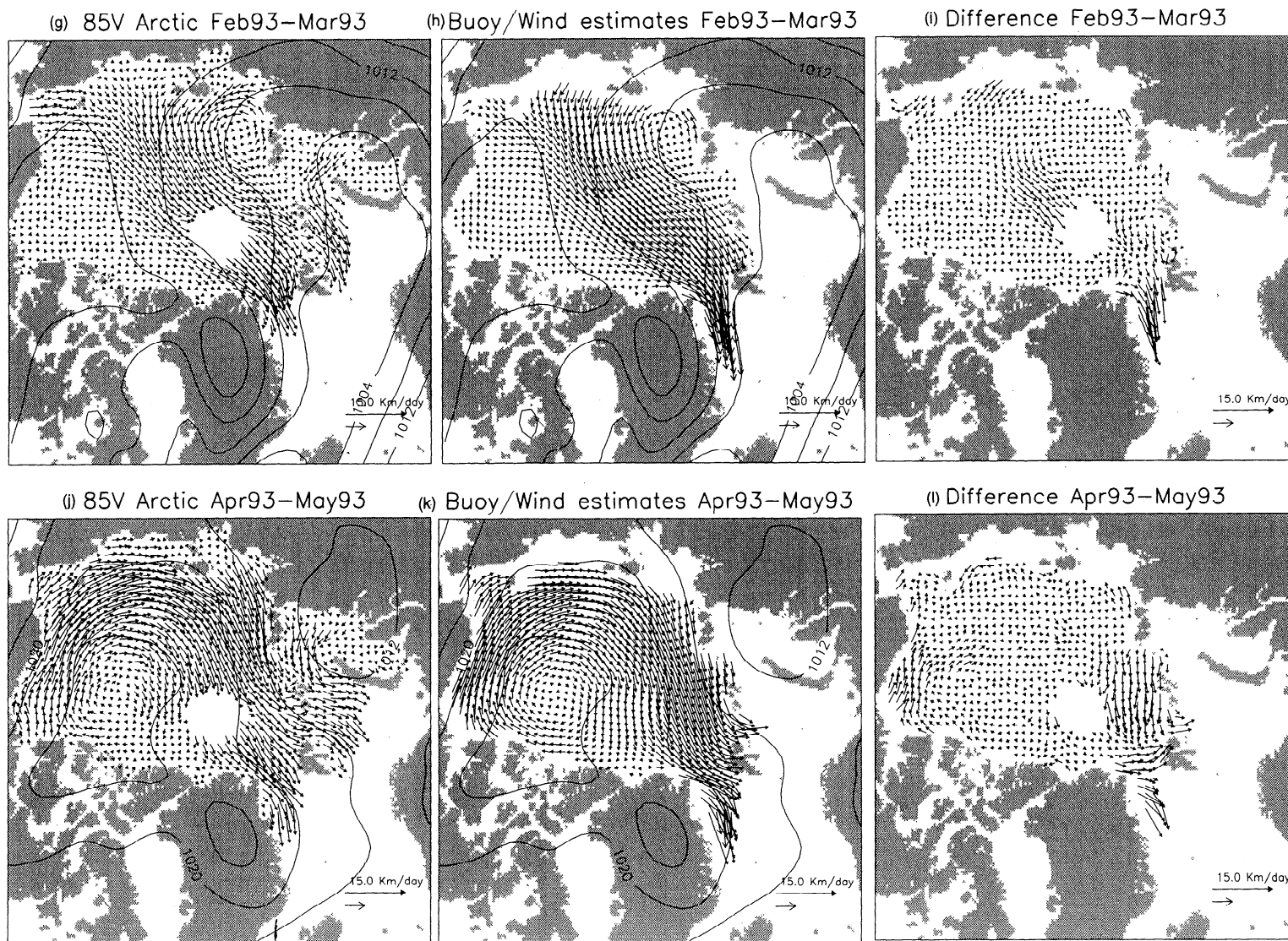
(a) 85V Arctic Oct92–Nov92   (b) Buoy/Wind estimates Oct92–Nov92   (c) Difference Oct92–Nov92

(d) 85V Arctic Dec92–Jan93   (e) Buoy/Wind estimates Dec92–Jan93   (f) Difference Dec92–Jan93

Figure 12. Comparison of the 85-GHz ice motion with interpolated buoy/wind motion field. The difference fields represent $u_{buoy/wind} - u_{SSM/I}$, that is, the buoy wind displacement minus the SSM/I displacement. The pressure contour interval is 4 mbar. Grid spacing is 80 km. (a) Two-month motion (October–November 1992) from SSM/I, (b) 2-month motion (October–November 1992) from buoy/wind estimates, (c) difference field (October–November 1992), (d) 2-month motion (December 1992 to January 1993) from SSM/I, (e) 2-month motion (December 1992 to January 1993) from buoy/wind estimates, (f) difference field (December 1992 to January 1993), (g) 2-month motion (February–March 1993) from SSM/I, (h) 2-month motion (February–March 1993) from buoy/wind estimates, (i) difference field (February–March 1993), (j) 2-month motion (April–May 1993) from SSM/I, (k) 2-month motion (April–May 1993) from buoy/wind estimates, and (l) difference field (April–May 1993).
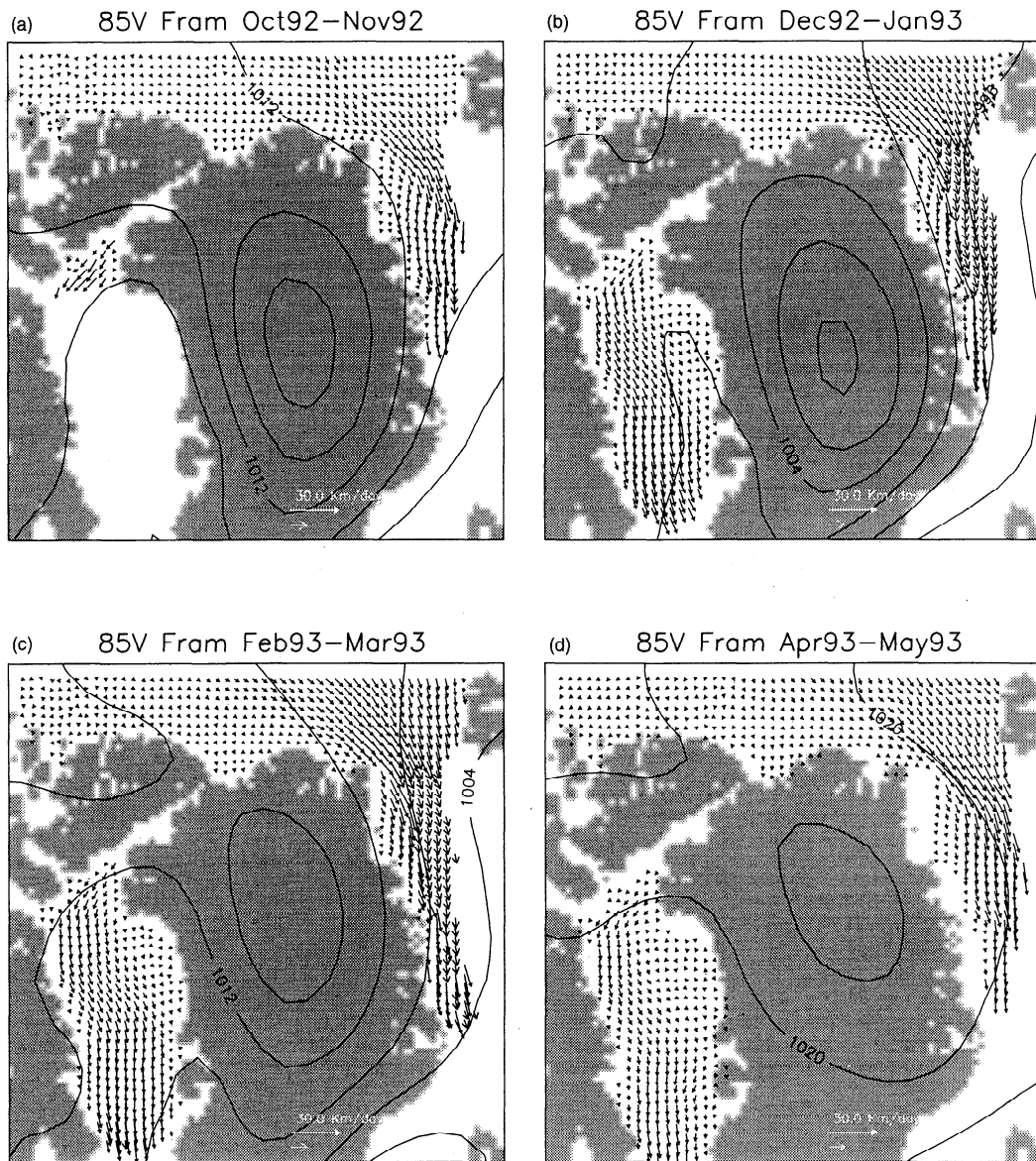
(g) 85V Arctic Feb93—Mar93   (h) Buoy/Wind estimates Feb93—Mar93   (i) Difference Feb93—Mar93

(j) 85V Arctic Apr93—May93   (k) Buoy/Wind estimates Apr93—May93   (l) Difference Apr93—May93

Figure 12. (continued)

Figure 13. Averaged bimonthly ice motion (Fram Strait/Baffin Bay) between October 1992 and May 1993. The pressure contour interval is 4 mbar. The grid spacing is 40 km. (a) Two-month motion (October–November 1992) from SSM/I, (b) 2-month motion (December 1992 to January 1993) from SSM/I, (c) 2-month motion (February–March 1993) from SSM/I, and (d) 2-month motion (April–May 1993) from SSM/I.

different view of the drift pattern. Figure 12b shows a situation with a saddle point in the pressure field in the Chukchi Sea. Any inaccuracy in the placement of the saddle causes the structure of the wind inputs to the buoy/wind estimate to cause some error. This case shows clearly the buoy/wind overestimate of ice flux through Fram Strait. Notice too that the SSM/I motions show a distinct immobile region with distinct edges in the Lincoln Sea, whereas the buoy/wind estimate has smoothed this stagnated region. Figure 12d shows a buoy/wind estimate of a field of motion for April and May of 1993 in which the pressure field consists of a well-developed anticyclone, not unlike the long-term mean field, and the ice motion is fairly vigorous everywhere. The smoothness in the field is due to the rather long length scale assumed in the optimal interpolation. The comparable ice motion derived by tracking SSM/I shows more spatial structure, particularly near Spitzbergen and Franz

Josef Land. Note the existence of SSM/I-tracked motion data in coastal regions of the Siberian shelf and in the Barents and Kara Seas, where buoy data are virtually absent. The difference field in Figure 12 (which can only be computed where both data sets contain data) shows that in some regions, particularly in Fram Strait, the buoy/wind estimates are too strong. This is thought to be due to the use of wind drift to estimate motions where buoy data are absent and ice stresses impede ice motion and invalidate the "free drift" approximation by which wind data are incorporated into the buoy/wind optimal interpolation. The motion differences between buoy/wind estimates and the SSM/I estimates near the passages between Severnaya Zemlya, Franz Josef Land and Svalbard are most pronounced in Figure 12d. The buoy/wind estimates assume unconstrained flow around the islands and seem to overestimate the motion in this situation.
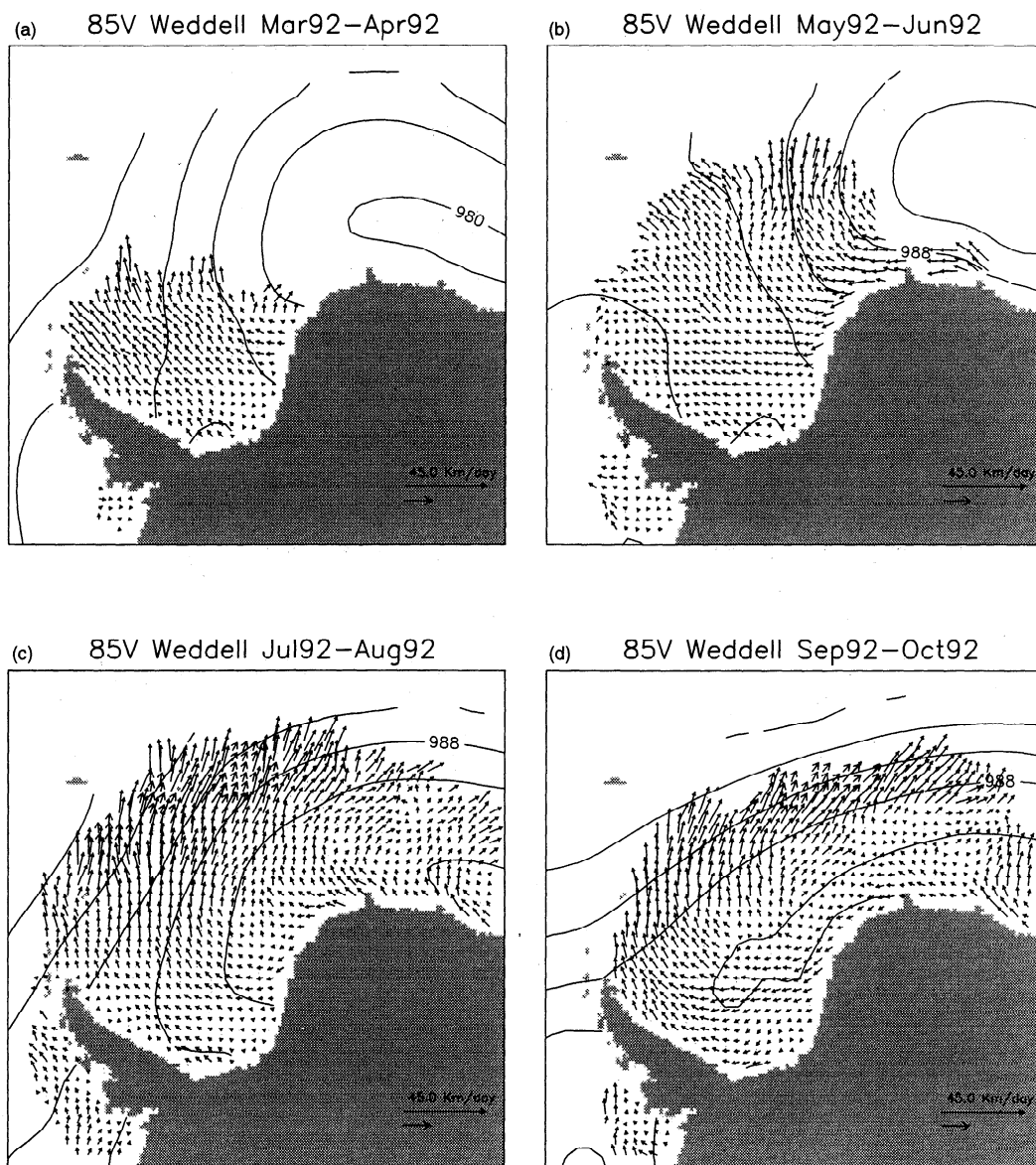
Figure 14. Averaged bimonthly ice motion (Weddell Sea) between March and October 1992. The pressure contour interval is 4 mbar. The grid spacing is 80 km. (a) Two-month motion (March–April 1992) from SSM/I, (b) 2-month motion (May–June 1992) from SSM/I, (c) 2-month motion (July–August 1992) from SSM/I, and (d) 2-month motion (September–October 1992) from SSM/I.

4.3. Fram Strait/Baffin Bay and Weddell Sea

The bimonthly mean sea ice motion in Fram Strait and Baffin Bay are depicted in Figure 13. An increase in the velocity of the sea ice is characteristic of the drift through the Fram Strait. Over the northeastern continental shelves of Greenland an anticyclonic feature of sea ice circulation can be observed. Mean motion north of Ellesmere Island is relatively small during all four periods. The ice motion west of Spitsbergen tends to be southwest and merges with the drift pattern through the Strait. The motion through the Strait is generally divergent. The ice motion in Baffin Bay is rather large, and the drift pattern is along the east coast of Baffin Island and southward toward Davis Strait into the Labrador Sea. On the west coast of Greenland the motion tends to be northwest but joins with the southward drift stream in Baffin Bay.

The net motion of sea ice in the Weddell Sea is shown in Figure 14. The large-scale circulation pattern of sea ice in the Weddell Sea is not as well-characterized as the drift patterns in the Arctic Basin. The cyclonic circulation of sea ice, known as the Weddell Gyre, is a major feature in this region. East of the Antarctic Peninsula, the net ice drift is to the north along the peninsula, and the sea ice tends to turn east as it gets entrained in the Antarctic Circumpolar Current. Because of the persistent motion north and away from the coast the motion is highly divergent as new and old ice are carried northward.

5. Summary/Discussion

We have demonstrated that ice motion can be obtained not only from 85-GHz SSM/I data but also from the lower-resolution 37-GHz data. By comparing 8 months of SSM/I-derived motions with contemporaneous buoy and SAR ice
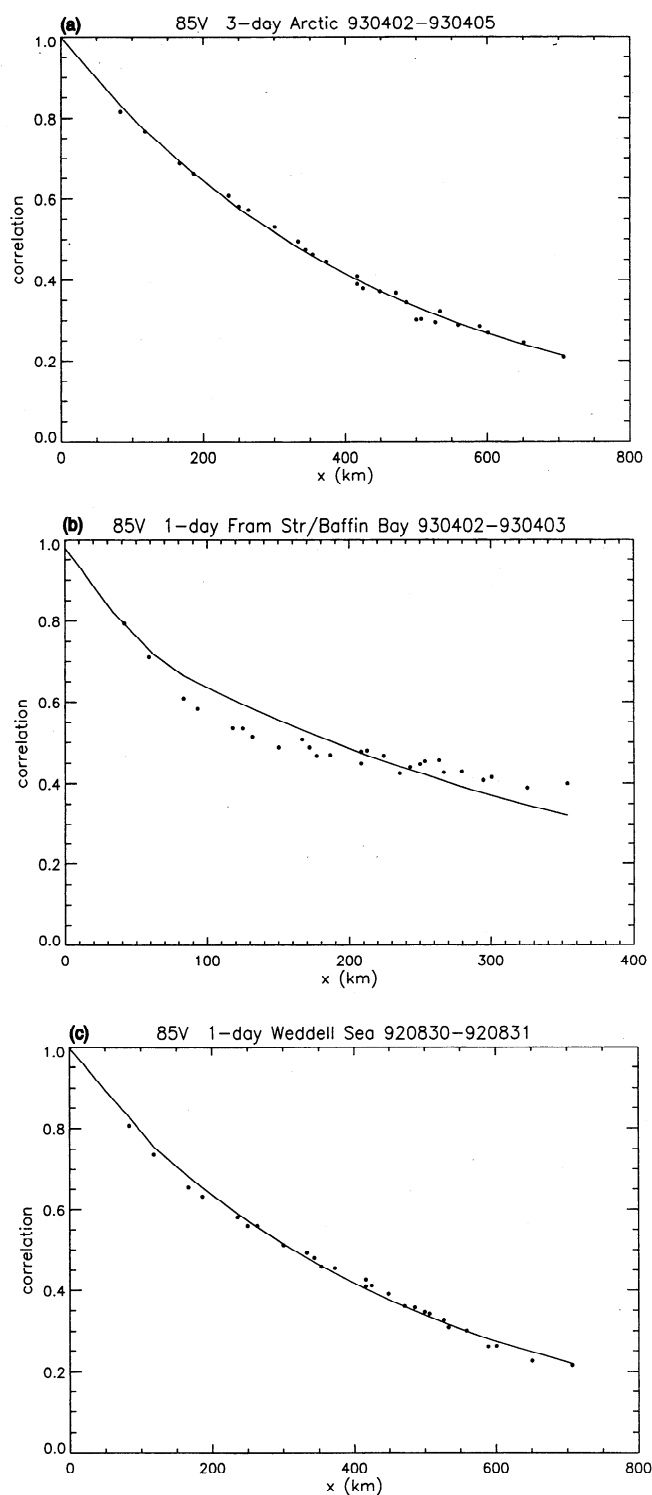
characterized as unbiased additive Gaussian noise, as suggested by the data here, then averaging would reduce the noise contribution to the estimates of mean motion; the decrease being proportional to $1/\sqrt{N}$, where N is the number of observations averaged in the mean displacement. For example, a weekly average of daily motion fields would reduce the standard deviation by a factor of 2.6. Our bimonthly averages of 3-day displacements reduce the standard deviation by a factor of 4.5. An alternate approach is to increase the displacement signal by lengthening the time interval between observations. There are a number of alternatives for tracking ice motion with the passive microwave data sets; we believe that regionally subsetting the gridded daily fields of brightness temperature for motion analysis would yield the best results. This approach would allow one to select spatial and temporal sampling parameters to maximize the signal-to-noise ratio based on our understanding of the ice motion in each region. The currently available daily gridded SSM/I data sets are not ideal for ice motion analysis because the "drop in the bucket" sampling procedure averages observations over a day and somewhat smears the spatial resolution. Any ice motion tends to distort the brightness temperature field and introduces an error that depends on the magnitude of ice motion giving spatially nonuniform error statistics. Orbital data would better preserve the location and time of each observation.

Given the quality of the passive microwave motion estimates, these data sets are best used for the understanding of the synoptic and longer-term drift patterns rather than the detailed characteristics of daily motion. The daily fields, without further filtering, are not well-suited for computing daily deformation (e.g., divergence, shear, etc.) because the errors would be intolerable. Averaged fields are more suitable for computation of longer-term deformation.

In spite of these limitations the motion fields show spatial details not previously observable. We see flows near the coast that buoys have never provided; in fact, motion fields estimated from buoy motions and winds tend to overestimate many coastal flows. The exchange of ice between the Arctic Ocean and its peripheral seas is newly observable. There are approximately 20 years of SMMR and SSM/I data. The feasibility of extracting ice motion from 85- and 37-GHz data offers an extraordinary opportunity to create an ice motion data record starting in 1978 and continuing through the present and indefinitely into the future with planned SSM/I and other passive microwave instruments.

Figure 15. Sample autocovariance functions from the three regions: (a) Arctic, (b) Fram Strait/Baffin Bay, and (c) Weddell Sea.

motion observations, we find that the standard deviation of the sampling error ranges between 5 and 12 km. These errors are less than the nominal resolutions (12 and 25 km) of the two radiometer channels. Even though the uncertainties are substantial compared to daily ice displacements, the patterns and trajectories of ice drift are represented well in the 8 months of data that we have examined. If these uncertainties can be

References

Agnew, T., H. Le, and T. Hirose, Estimation of large scale sea ice motion from SSM/I 85.5 GHz imagery, *Ann. Glaciol.*, in press, 1997.

Emery, W. J., C. W. Fowler, J. Hawkins, and R. H. Preller, Fram Strait satellite image-derived ice motions, *J. Geophys. Res.*, *96*(C5), 8917–8920, 1991.

Fily, M., and D. A. Rothrock, Sea ice tracking by nested correlations, *IEEE Trans. Geosci. Remote Sens.*, *GE-25*(5), 570–580, 1987.

Goodberlet, M. A., Special sensor microwave/imager calibration/validation, Ph.D. thesis, Univ. of Mass., Amherst, 1990.

Holt, B., D. A. Rothrock and R. Kwok, Determination of sea ice motion from satellite images, in *Microwave Remote Sensing of Sea Ice, Geophys. Monogr. Ser.*, vol. 68, edited by F. D. Carsey, pp. 344–354, AGU, Washington, D. C., 1992.

Kottmeier, C., J. Olf, W. Freiden, and R. Roth, Wind forcing and ice motion in the Weddell Sea region, *J. Geophys. Res.*, *97*(D18), 20,373–20,383, 1992.

Kwok, R., and G. F. Cunningham, Geophysical processor system data users guide, *Doc. D-9526*, Jet Propul. Lab., Pasadena, Calif., 1993.

Kwok, R., J. C. Curlander, R. McConnell, and S. Pang. An ice motion tracking system at the Alaska SAR facility, *IEEE J. Oceanic Engineering*, *15*(1), 44–54, 1990.

Liu, A., D. J. Cavalieri, and C. Y. Peng, Sea ice drift from wavelet analysis of DMSP SSM/I data, *Int. J. Remote Sens.*, in press, 1998.

Pfirman, S. L., R. Colony, D. Nürnberg, H. Eichen, and I. Rigor, Reconstructing the origin and trajectory of drifting Arctic sea ice, *J. Geophys. Res.*, *102*(C6), 12,575–12,586, 1997.

Rigor, I., and A. Heiberg, International arctic buoy program data report, 1 January 1996–31 December 1996, *Rep. APL-UW TM 05-97*, Appl. Phys. Lab., Univ. of Wash., Seattle, 1997.

Thorndike, A. S., Kinematics of sea ice, in *The Geophysics of Sea Ice*, edited by N. Untersteiner, *NATO ASI Ser., Ser. B*, *146*, 489–550, 1984.

Thorndike, A. S., and R. Colony, Arctic ocean buoy program, 19 January 1979–31 December 1979, data report, Polar Sci. Cent., Univ. of Wash., Seattle, 1980.

C. Kottmeier, Universität Karlsruhe, Institut für Meteorologie und Klimaforschung, Kaiserstrasse 12 (Physikhochhaus), 76128 Karlsruhe, Germany.

R. Kwok and S. Pang, Jet Propulsion Laboratory, California Institute of Technology, 4800 Oak Grove Drive, Pasadena, CA 91109. (e-mail: ron@rgps1.jpl.nasa.gov)

D. A. Rothrock and A. Schweiger, Polar Science Center, Applied Physics Laboratory, College of Ocean and Fisheries Sciences, University of Washington, Seattle, WA 98195.